Functional Localization of the Human Auditory and Visual Thalamus Using a Thalamic Localizer Functional Magnetic Resonance Imaging Task

John C. Williams[1,2], Philip N. Tubiolo[1,2], Zu Jie Zheng[1,3], Eilon B. Silver-Frankel[1], Dathy T. Pham[1,6], Natalka K. Haubold[1], Sameera K. Abeykoon[1], Anissa Abi-Dargham[1,2,4,5,7], Guillermo Horga[4,5], and Jared X. Van Snellenberg[1,2,4,5,8,*]

Affiliations

[1]Department of Psychiatry and Behavioral Health, Renaissance School of Medicine at Stony Brook University, Stony Brook, NY 11794;

[2]Department of Biomedical Engineering, Stony Brook University, Stony Brook, NY 11794;

[3]State University of New York Downstate Health Sciences University College of Medicine, Brooklyn, NY 11203;

[4]Department of Psychiatry, Columbia University Vagelos College of Physicians and Surgeons, New York-Presbyterian / Columbia University Irving Medical Center, New York, NY 10032;

[5]New York State Psychiatric Institute, New York, NY 10032;

[6]Department of Neurobiology and Behavior, Cornell University, Ithaca, NY 14853;

[7]Department of Radiology, Renaissance School of Medicine at Stony Brook University, Stony Brook, NY 11794;

[8]Department of Psychology, Stony Brook University, Stony Brook, NY 11794.

*To whom correspondence may be addressed.

Email: Jared.VanSnellenberg@stonybrookmedicine.edu

Address: 101 Nicolls Rd., Health Sciences Center T10-087J, Stony Brook, NY 11794

Short/running title: fMRI Localization of the Human Auditory and Visual Thalamus

Keywords: Auditory processing; visual processing; medial geniculate; lateral geniculate; functional localizer task; resting-state functional connectivity

The main text of this manuscript includes the following display items:

- Figures 1 to 6
- Table 1

Abstract

Functional magnetic resonance imaging (fMRI) of the auditory and visual sensory systems of the human brain is an active area of investigation in the study of human health and disease. The medial geniculate nucleus (MGN) and lateral geniculate nucleus (LGN) are key thalamic nuclei involved in the processing and relay of auditory and visual information, respectively, and are the subject of blood-oxygen-level-dependent (BOLD) fMRI studies of neural activation and functional connectivity in human participants. However, localization of BOLD fMRI signal originating from neural activity in MGN and LGN remains a technical challenge, due in part to the poor definition of boundaries of these thalamic nuclei in standard T1-weighted and T2-weighted magnetic resonance imaging sequences. Here, we report the development and evaluation of an auditory and visual sensory thalamic localizer (TL) fMRI task that produces participant-specific functionally-defined regions of interest (fROIs) of both MGN and LGN, using 3 Tesla multiband fMRI and a clustered-sparse temporal acquisition sequence, in less than 16 minutes of scan time. We demonstrate the use of MGN and LGN fROIs obtained from the TL fMRI task in standard resting-state functional connectivity (RSFC) fMRI analyses in the same participants. In RSFC analyses, we validated the specificity of MGN and LGN fROIs for signals obtained from primary auditory and visual cortex, respectively, and benchmark their performance against alternative atlas- and segmentation-based localization methods. The TL fMRI task and analysis code (written in Presentation and MATLAB, respectively) have been made freely available to the wider research community.

1 Introduction

The thalamus is a key neural processing hub in human sensory perception (Kandel, 2013; Mai & Paxinos, 2012; Sherman, 2016; Ward, 2013). Disruption of thalamocortical connectivity has been implicated in the pathogenesis of multiple neurological and psychiatric diseases (Anticevic et al., 2014; Anticevic et al., 2015; Chun et al., 2017; Chun et al., 2014; Giraldo-Chica et al., 2018; Karlsgodt, 2016; Kelly et al., 2018; Kim et al., 2014; Kubota et al., 2013; Murray & Anticevic, 2017; Pasternak et al., 2018; Peters et al., 2016; Pettersson-Yeo et al., 2011; Sheffield et al., 2020; Tamnes & Agartz, 2016; Tu et al., 2019; Woodward & Cascio, 2015; Woodward et al., 2017; Woodward & Heckers, 2016; Woodward et al., 2012), including potential specific involvement of sensory thalamic nuclei (Chun et al., 2017; Chun et al., 2014; Giraldo-Chica et al., 2015; Huang et al., 2024). Accordingly, the study of neural activity in sensory thalamic nuclei and their functional connectivity with sensory cortex is an area of active investigation in the study of the human brain in health and disease (Almasabi et al., 2022; Bartlett, 2013; Chun et al., 2017; Chun et al., 2014; Erskine et al., 2016; Papadopoulou et al., 2019; Schmid et al., 2010; Truong et al., 2015), including through the use of blood-oxygen-level-dependent (BOLD) functional magnetic resonance imaging (fMRI) of human participants.

Within the thalamus, the medial geniculate nucleus (MGN) and lateral geniculate nucleus (LGN) are integral components of the human auditory and visual pathways, respectively, and play critical roles in the modulation and relay of incoming sensory information to the cortex (Kandel, 2013; Sherman, 2016; Ward, 2013). The MGN receives incoming sensory information from the cochlear nucleus, primarily through the

inferior colliculus and superior olivary complex, and provides ascending inputs to the auditory cortex (AC; Bartlett, 2013; Brodal, 1981; Kandel, 2013; Lee, 2013). The AC, in turn, projects distally back to MGN, inferior colliculus, and superior olive (Bartlett, 2013; Lee, 2013), in order to facilitate integration of modulatory and contextual information, such as prediction error signals (Li & Ebner, 2016; Malmierca et al., 2015; Parras et al., 2017). Similarly, the LGN receives inputs from the retina, as well as the superior colliculus, and provides inputs to the visual cortex (VC), which projects back to LGN and superior colliculus (Gilbert & Li, 2013; Lee et al., 2010; Sherman, 2016).

BOLD fMRI studies that aim to measure activity within MGN and LGN hinge upon accurate localization of these structures. However, identifying regions of interest (ROIs) within the thalamus that contain BOLD activation patterns specific to auditory and visual perception using standard atlases or segmentation techniques is hindered by the relatively small size of these nuclei (e.g., estimates of approximately 120 mm^3 and 60 mm^3, respectively, for LGN (Muller-Axt et al., 2021) and MGN (Garcia-Gomar et al., 2019)), and a lack of distinct anatomical landmarks in the posterior thalamus that can be identified using T1-weighted (T1w) and T2-weighted (T2w) imaging sequences that causes segmentation algorithms to rely heavily on priors (relative to individual-specific anatomical information). Moreover, individual variability in the location and size of nuclei (Andrews et al., 1997; Garcia-Gomar et al., 2019; Giraldo-Chica & Schneider, 2018; Kiwitz et al., 2022; Rademacher et al., 2002) is exacerbated by both the difficulty of precise spatial normalization to standardized spaces, and the resulting imprecision in the coregistration between anatomical structural images and echo planar images (EPIs) measuring hemodynamic BOLD signal.

One broadly successful approach to localizing brain regions with specific neural functions that are otherwise difficult to localize based on anatomical scans alone is to develop and utilize a task that specifically elicits the function subserved by the targeted neural region, commonly known as a functional localizer task (Berman et al., 2010; Dodell-Feder et al., 2011; Fedorenko et al., 2010; Jacoby et al., 2016; Jiang et al., 2013; Kastner et al., 2004; Saxe et al., 2006). Consequently, BOLD fMRI sensory thalamic localizer (TL) tasks have been developed to measure human sensory thalamic responses *in vivo*, enabling group-wide and/or single-participant localization of geniculi experimentally (Chen et al., 1998; Denison et al., 2014; Hess et al., 2009; Jiang et al., 2013; Kastner et al., 2004; Schneider & Kastner, 2009; Sitek et al., 2019).

In this work, we developed and implemented an auditory and visual sensory TL fMRI task, using high-resolution multiband fMRI (Moeller et al., 2010), with the aim of producing functionally-defined ROIs (fROIs) optimal for extracting information from other BOLD images acquired from the same participant. To improve functional specificity, this task uses clustered-sparse temporal acquisition (Schmidt et al., 2008; Yang et al., 2000; Zaehle et al., 2007), through which volumes are collected only immediately after the presentation of task stimuli, thereby reducing the confounding effect of concurrent scanner noise, which is critical when studying auditory processing with fMRI (Bandettini et al., 1998; Schmidt et al., 2008). The task developed here builds on prior sensory TL tasks by 1) combining both visual and auditory stimulation in a single task to simultaneously identify fROIs for MGN and LGN; 2) leveraging multiband acceleration to improve spatial resolution and increase the number of data points (volumes) acquired with each acquisition cluster, which in turn facilitates 3) using a shorter (~15 minute)

total task length while still obtaining high quality fROIs; and 4) is developed and tested at 3 Tesla (as opposed to higher fields) in order to maximize availability to investigators.

We report the utility of this sensory TL task in producing participant-level MGN and LGN fROIs, validate their specificity for auditory and visual processing using resting-state (RS) fMRI scans acquired from the same participants, and demonstrate the performance of these fROIs relative to widely used atlas and segmentation-based techniques. Code for the TL fMRI task employed here, as well as participant-level analysis code for generating MGN and LGN fROIs, are also made publicly available for use by the wider research community.

2 Materials and Methods

2.1 Overview

This is a two-site study of healthy participants who completed task procedures at either the New York State Psychiatric Institute (NYSPI) or Stony Brook University (SBU). All research procedures at NYSPI were approved by the New York State Psychiatric Institute Institutional Review Board; all research procedures at SBU were approved by the Stony Brook University Institutional Review Board. Participants were recruited with advertisements and all individuals provided written consent prior to their participation.

2.2 General Inclusion and Exclusion Criteria

Data at each site were collected from healthy adult participants, ages 18-55, over the course of other studies, and thus inclusion and exclusion criteria varied slightly between sites. Full inclusion and exclusion criteria for each site are described in the ***Inclusion and Exclusion Criteria*** section of **Supplementary Materials and Methods.**

All participants were free of any major neurological disorders, psychiatric disorders, current substance use disorders, and hearing impairment. Participants at SBU were additionally tested for normal hearing thresholds and speech recognition for monosyllabic words. Psychiatric diagnoses were determined at NYSPI according to the Diagnostic and Statistical Manual of Mental Disorders, Fourth Edition, Text Revision (DSM-IV-TR; American Psychiatric Association, 2000), and at SBU according to the Diagnostic and Statistical Manual of Mental Disorders, Fifth Edition (DSM-5; American Psychiatric Association, 2013).

2.3 Demographic and Clinical Assessments

Handedness was assessed using the Edinburgh Handedness Inventory (EHI; Oldfield, 1971), and socioeconomic status using the Hollingshead Four Factor Index of Socioeconomic Status (Hollingshead, 1975). Family history of mental disorders was assessed using the Family History Screen (FHS; Milne et al., 2009). Clinical measures were assessed at NYSPI using the Structured Clinical Interview for the DSM-IV Axis I Disorders (SCID-I; First & Gibbon, 2004), and at SBU using the Structured Clinical Interview for DSM-5, Research Version (SCID-5-RV; First et al., 2015), and at both sites using the Positive and Negative Syndrome Scale (PANSS; Kay et al., 1987). At SBU, hearing thresholds were evaluated either using a GSI Automated Method for Testing Auditory Sensitivity Pro (Grason-Stadler, Eden Prairie, Minnesota) automated audiometry system, or by a licensed audiologist or otolaryngologist, and speech recognition for monosyllabic words using the Northwestern University Auditory Test No. 6 (Carhart & Tillman, 1966).

2.4 fMRI Acquisition

Prior to magnetic resonance (MR) scanning procedures, participants completed an MRI clearance form to assess for metallic implants and past experiences with metal, and were administered a urine toxicology test, as well as a urine pregnancy screen for biologically female participants. MR scanning was carried out using a 3 Tesla General Electric (GE; Boston, MA) MR750 with a NOVA 32-channel head coil at NYSPI, and a 3 Tesla Siemens (Munich, Germany) MAGNETOM Prisma at the SBU Social, Cognitive, and Affective Neuroscience (SCAN) Center with a Siemens 64-channel head-and-neck coil (Keil et al., 2013). All T2* BOLD EPI data were acquired in alternating, opposing phase-encode (PE) directions, i.e., two anterior-posterior (AP) PE runs and two posterior-anterior (PA) PE runs.

The following data were acquired during each session at SBU: 1) high-resolution (0.80 mm isotropic voxels) anatomical T1w and T2w scans; 2) four T2*-weighted BOLD EPI RS runs; 3) four T2*-weighted BOLD EPI TL runs; 4) two spin echo field maps, one AP and one PA; and 5) one B0 field map. BOLD fMRI data were acquired at NYSPI with a TR of 850 ms and field of view of 192 mm, while BOLD data acquired at SBU were acquired with a TR of 800 ms and field of view of 204 mm. BOLD data were acquired from both sites with 2mm isotropic voxels, a flip angle of 60 degrees, echo time of 25 ms, and multiband factor of 6. The duration of each RS run was 7 minutes 34 seconds at NYSPI and 7 minutes 38 seconds at SBU. At both sites (NYSPI and SBU), each thalamic localizer run was 3 minutes 46 seconds in duration. Participants were asked to complete 4 runs each of the TL fMRI task and RS fMRI, with a minimum of two runs of each required for study completion and inclusion in the final analyzed dataset.

2.5 Sensory Thalamic Localizer fMRI Task Procedures

The goal of the sensory thalamic localizer task is to identify regions of the thalamus specifically responsive to auditory and visual stimuli in each participant, as has been done in prior work (Jiang et al., 2013; Kastner et al., 2004). This task uses clustered-sparse temporal acquisition (Schmidt et al., 2008; Yang et al., 2000; Zaehle et al., 2007), in which fMRI volumes are not acquired while task stimuli are presented. Instead, fMRI is acquired immediately after the presentation of stimuli, in order to minimize the effect of scanner noise from BOLD data acquired; otherwise, the sound produced by the MR scanner while volumes are being acquired could confound detected responses to stimuli (Schmidt et al., 2008). In this task, 3 volumes of BOLD fMRI are acquired at the end of each trial. Acquisition clusters were timed such that a) the hemodynamic response to scanner noise produced by the prior acquisition cluster should have returned to baseline levels, and b) the hemodynamic response to stimuli presented between two clusters is at or near its peak when the acquisition cluster is acquired.

A schematic diagram of the sensory TL fMRI task is shown in **Figure 1.** In each run **(Figure 1A)**, participants are presented with 16 trials of either visual or auditory stimulation in a pseudorandom order. Each trial consists first of a “gap period” of silence, 9 seconds of stimulation (sufficient to reach the peak of the hemodynamic response in sensory cortex; Inan et al., 2004; Jiang et al., 2013), a second “gap period” of silence equal in duration to the first, and then the clustered acquisition of 3 volumes of BOLD data (TR × 3 in duration). The duration of gap periods is calibrated such that the total trial time is 12 seconds in both NYSPI and SBU data, where the acquisition clusters last 3 TRs. In NYSPI data, this gap period is 225 ms (acquisition cluster

duration of 2.55 s); in SBU data, this gap period is 300 ms (acquisition cluster duration of 2.4 s).

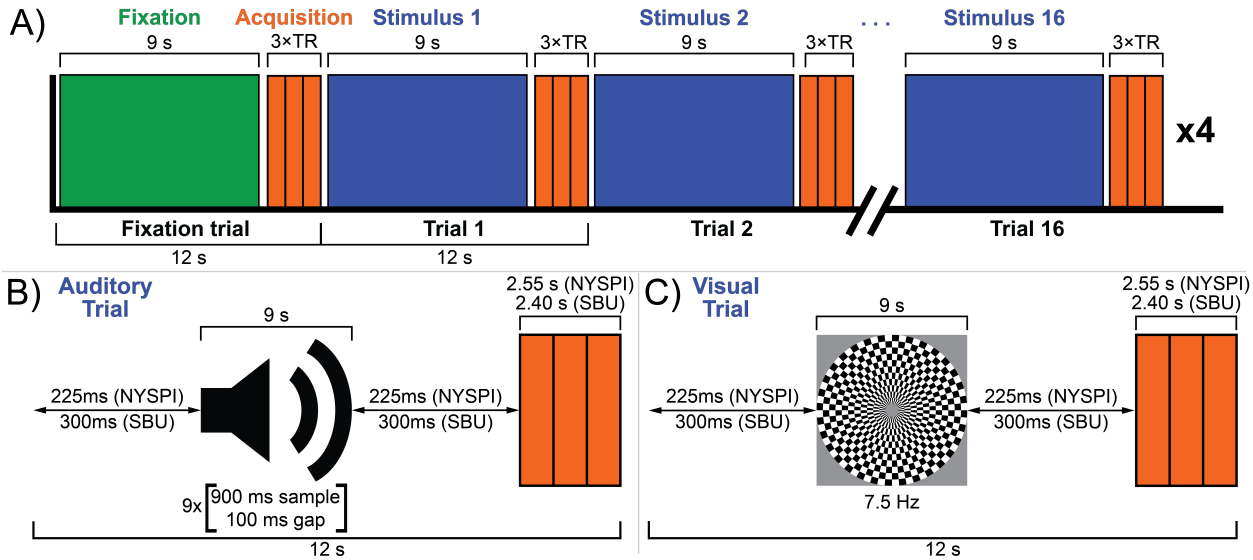

Figure 1. The sensory thalamic localizer (TL) task. A schematic diagram of a TL task run is shown in panel **A**. Each run begins with a single 12-second fixation trial (green), followed by sixteen 12-second stimulus trials, consisting of 8 auditory and 8 visual trials (blue), presented in pseudorandom order, using clustered-sparse temporal acquisition. Sample auditory and visual trials are respectively shown in panels **B** and **C.** Each trial consists of 9 seconds of stimulation, followed by a single acquisition cluster of 3 volumes (orange). Acquisition clusters are 3 TRs in duration, totaling 2.55 s in NYSPI data and 2.4 s in SBU data. Stimuli are immediately preceded and succeeded by gaps of equal duration, during which no stimulus is presented, in order to bring the total trial time to 12 seconds; this gap time is 225 ms in NYSPI data and 300 ms in SBU data. Auditory trials consist of nine sets of 900 ms amplitude-normalized snippets of instrumental music presented in pseudorandom order and separated by 100 ms gaps. Visual trials consist of a circular checkerboard alternating between black and white at 7.5 Hz. Participants were asked to complete a total of 4 task runs.

Auditory stimulation was presented as nine sets of 900 ms segments of music, followed by 100 ms of silence, in pseudorandom order **(Figure 1B),** similar to prior work (Jiang et al., 2013), in order to reduce neural responses specific to the experience of listening to music, delivered binaurally using a SereneSound headset and transducer (Resonance Technology, Inc., Northridge, CA)**.** Musical segments were obtained from the instrumental song, *Transmission94 (Parts 1 & 2)* by *Bonobo.* This song was chosen to meet the following criteria: 1) instrumental music, to avoid evoking responses specific to speech processing in segments containing perceptible speech fragments; 2) no

breaks or pauses in the music; and 3) a long enough song to produce at least 7.5 minutes of audio segments after discarding the first and last 4.8 seconds of the song (to avoid fade in/fade out effects or segments in which the music begins late or ends early; also note that less than 7.5 minutes was ultimately used in the task version reported here). Musical segments were normalized to have the same mean amplitudes in order to avoid sudden changes in amplitude when the presentation switches from one 900 ms segment to another (which may have been selected from disparate portions of the song).

Visual stimulation was presented via a projector with a 60 Hz refresh rate as a circular black-and-white checkerboard with a central fixation cross, alternating between light and dark with a reversal frequency of 7.5 Hz **(Figure 1C),** which was found in prior work to reliably activate both LGN and VC (Kastner et al., 2004; Kastner et al., 2006; Rosa et al., 2010)**.** The presentation of task stimuli was controlled using Presentation software (Version 22.1, Build 10.23.20, Neurobehavioral Systems, Inc., Berkeley, CA, www.neurobs.com) installed on a dedicated laptop. The sensory TL task Presentation code (Williams et al., 2024) is freely available from the Neurobehavioral Systems Archives of Neurobehavioral Experiments and Stimuli at http://www.neurobs.com/ex_files/expt_view?id=302.

2.6 Resting-State fMRI Procedures

During RS scans, participants were instructed to look ahead at a fixation cross, remaining still and awake with their eyes open. One of the participants' eyes was monitored by a research coordinator via an eye tracking camera (although eye tracking was not collected), and eye closure times were recorded to exclude times from analysis

times during which participants may have been sleeping, as participants entering into and out of sleep states has been shown to measurably impact on measured RSFC (Tagliazucchi & Laufs, 2014).

2.7 fMRI Pre-Processing and Post-Processing

All fMRI data were preprocessed through the following steps of the Human Connectome Project Minimal Preprocessing Pipelines (HCP MPP; Glasser et al., 2013), version 4.2.0 (https://github.com/Washington-University/HCPpipelines): 1) *PreFreeSurfer*, 2) *FreeSurfer*, 3) *PostFreeSurfer,* and 4) *fMRIVolume*. Surface registration was completed by cortical surface matching (MSMsulc; Robinson et al., 2018; Robinson et al., 2014). Preprocessed structural (T1w) and functional (BOLD) images were obtained from *fMRIVolume* normalized to Montreal Neurological Institute (MNI) 152 non-linear 6th-generation space (MNI152NLin6; Grabner et al., 2006).

Nuisance signals for white matter (WM) and cerebro-spinal fluid (CSF) were calculated in unsmoothed data as the average signal in all compartment voxels that remain after an iterative erosion procedure (Power et al., 2014). In this iterative erosion procedure, masks are eroded up to three times, as long as one additional erosion would result in at least two remaining voxels. Six vectors of motion parameters (MPs), the estimated framewise motion in each of the 3 directions of translation and 3 directions of rotation, was also obtained from the HCP MPP. TL and RS BOLD fMRI data were smoothed using a 4 mm full-width-half-maximum Gaussian filter (note that unsmoothed data was retained and used in analyses where noted below).

2.7.1 Resting-State fMRI Data Post-Processing

RS images (both smoothed and unsmoothed) were mode 1000 normalized

(divided by the modal value of all in-brain voxels and multiplied by 1000; Power et al., 2012), linearly detrended, and mean centered. Volumes acquired during periods of excess participant motion were removed using volume censoring. Volume censoring (Power et al., 2012; Power et al., 2014; Power et al., 2015; Smyser et al., 2011; Williams et al., 2022) was performed using study-wide thresholds for participant motion, measured by low-pass-filtered framewise displacement (LPF-FD), and run-wise thresholds for whole-brain signal fluctuation, using generalized extreme value low-pass filtered temporal derivative root-mean-squared over voxels (GEV-DV) thresholding, as has been described in detail elsewhere (Williams et al., 2022). Censoring thresholds were determined using resting-state data available for participants with usable TL MGN and LGN fROIs using the Multiband Censoring Optimization Tool (Williams et al., 2022) (https://github.com/CNaP-Lab/MCOT/), resulting in an LPF-FD threshold (Φ_F) of 0.07587 mm and GEV-DV parameter (d_G) of 3.105 (arbitrary units).

Volumes acquired at times during which a participant eye closure lasted longer than 3 seconds in duration were additionally removed through volume censoring, as were volumes acquired between eye closure periods that occurred less than 30 seconds apart. Contiguous clusters of data that were less than 8 s in duration after censoring were discarded, as were resting state runs with fewer than 1.5 minutes of remaining data. Participants with fewer than either 2 runs of data remaining, or fewer than 5 minutes of remaining data in total, were excluded from resting-state analyses.

RS runs were filtered using a 0.009-0.08 Hz band-pass second-order zero-phase Butterworth filter, with censored time points replaced by linear interpolation prior to band-pass filtering before being discarded from analysis. The first and last 22 seconds

of each time series were discarded to remove discontinuity (edge) artifacts present after band-pass filtering; approximately 22 seconds of data were removed from the start and end of each run (slightly different between sites due to the different TRs: 22.1 s / 26 volumes at NYSPI, 22.4 s / 28 volumes at SBU).

2.8 Sensory Thalamic Localizer fMRI Task Analysis

2.8.1 Overview

The objective in analyzing the TL task is to identify voxels within defined regions of posterior thalamus that show coactivation with either auditory cortex or visual cortex, but not both, over the course of alternating auditory and visual stimulation. To achieve this, TL task data were analyzed to first identify a cluster within each hemisphere's auditory cortex (AC) and visual cortex (VC) that was maximally responsive to either auditory or visual stimulation, respectively (section **2.8.3**). Average AC and VC time series were extracted from these clusters (section **2.8.4**).

Participant-specific hemispheric thalamic search region (TSR) masks for MGN and LGN (MGN-TSR and LGN-TSR, respectively) were generated (section **2.8.2**). Voxels within the MGN-TSR and LGN-TSR were assessed for coactivation with the AC and VC time series during the TL task (using Pearson's partial correlations; see section **2.8.5)** and thresholded based on this coactivation. Voxels showing coactivation with both AC and VC time series were removed to improve specificity (section **2.8.5)**. The largest remaining contiguous cluster within each hemisphere's MGN-TSR and LGN-TSR were extracted as each participant's MGN and LGN, respectively.

2.8.2 *A Priori* Regions of Interest

Auditory cortex (AC) and visual cortex (VC) search region masks were generated

from Brodmann areas (BAs) using the Wake Forest University PickAtlas Toolbox (WFU; Maldjian et al., 2004; Maldjian et al., 2003). A temporal lobe AC mask was produced from BAs 41 and 42, and an occipital lobe VC mask from BAs 17 and 18, and each was finally dilated in 3D by one voxel.

Hemispheric search region masks for auditory thalamus (MGN-TSR) and visual thalamus (LGN-TSR) were generated for each participant by first applying the FreeSurfer thalamic nuclei segmentation (Iglesias et al., 2018) to each participant's anterior commissure-posterior commissure (AC-PC) aligned, readout distortion and bias field corrected T1w image. The resulting segmentation output image was warped to MNI152NLin6 space using the warps calculated by the HCP MPP (*acpc_dc2standard.nii.gz*) and resampling to BOLD space, using Connectome Workbench 1.5.0 (Marcus et al., 2011) (*wb_command -volume-resample*). To create an appropriately large search space in posterior thalamus, FreeSurfer estimates of MGN were 3D dilated 3 voxels for the MGN-TSR, and FreeSurfer estimates of LGN were 3D dilated by 1 voxel for the LGN-TSR (as the FreeSurfer LGN ROIs were slightly larger).

To help ensure that fROIs were distinct from surrounding structures, TSR voxels estimated to comprise part of surrounding structures were removed to improve specificity and robustness across participants as follows. First, masks of pulvinar and mediodorsal nuclei were obtained from the FreeSurfer thalamic segmentation. Next, the following masks were obtained from the FreeSurfer segmentation atlas (Desikan et al., 2006; Fischl, 2012; Fischl et al., 2004) output by the HCP MPP (*Atlas_wmparc.2.nii.gz*): cortical gray matter, parahippocampal gyrus WM, insular cortex WM, choroid plexus, pulvinar, mediodorsal nucleus, putamen, pallidum, and hippocampus. The masks of

mediodorsal nucleus, insular cortex WM, choroid plexus, pulvinar, mediodorsal nucleus, putamen, and pallidum were 3D dilated by 1 voxel. All voxels overlapping with masks of surrounding structures were then removed from MGN-TSR and LGN-TSR masks. Finally, the posterior-most 2 slices of each TSR mask were then removed to remove voxels in close proximity to midbrain, and any MGN-TSR voxels superior to the inferior-most slice of the pulvinar in either hemisphere were removed to constrain the search region to the inferior aspect of posterior thalamus and remove remaining voxels posterior to the pulvinar FreeSurfer ROI. Probability maps of final MGN-TSR and LGN-TSR masks are shown in **Figure S1.**

2.8.3 Generalized Linear Modeling and Generation of Participant-Level Contrasts

Smoothed TL task fMRI data were analyzed using a generalized linear modeling framework in SPM12 (Friston et al., 2007; Friston, Holmes, et al., 1994; Friston, Jezzard, et al., 1994), version 7771, in MATLAB R2018a (The MathWorks, Inc., Natick, MA), with betas estimated from a design matrix that contained, for each run, a column each for intercept, auditory stimulation, visual stimulation, 6 MPs and their squares, WM signal, and CSF signal, as well as two additional regressors to model the second and third volumes of each cluster. These volume-specific regressors were employed to regress out the effect of T1-relaxation on BOLD signal, as the clustered-sparse temporal acquisition scheme meant that BOLD data were not at steady-state during acquisition (Horga et al., 2014; Schmidt et al., 2008; Zaehle et al., 2007). Task regressors indicating trial type (auditory or visual) were not convolved with a hemodynamic response function (HRF), because the sparse temporal sampling

precludes a true timeseries HRF model, as acquisition of volumes is not continuous.

Contrast images of activation from auditory stimulation versus visual stimulation (Auditory − Visual) were then generated for each participant. Each hemisphere's AC search region masks were thresholded to include only voxels with the top 10% of [Auditory − Visual] contrast values, and VC search region masks were similarly thresholded to include only the bottom 10% of [Auditory − Visual] contrast values. Clusters smaller than 10 contiguous voxels in size were then removed. The single, contiguous cluster within each AC mask and VC mask with the greatest magnitude peak contrast value was used for extraction of AC and VC task time series.

2.8.4 Extraction of Time Series

To obtain AC and VC time series for each participant, TL task BOLD activation was averaged within each hemisphere's AC and VC clusters, as identified in section **2.8.3**. These hemispheric AC and VC time series were then averaged across hemispheres, resulting in single AC and VC time series for each participant.

Local WM signal was additionally obtained for each TSR for use as nuisance regressors by first identifying WM in the FreeSurfer segmentation atlas located between 1 and 5 voxels from the TSR in any direction, and then extracting average time series from these voxels from unsmoothed BOLD data. Brain-wide gray matter signal was extracted by eroding the FreeSurfer segmentation atlas by one voxel and spatially averaging signal from unsmoothed BOLD data within the resultant mask.

2.8.5 Task Coactivation Analysis and Identification of MGN and LGN Regions of Interest

We aimed to identify thalamic voxels in each TSR that coactivate, over the

course of auditory and visual stimulation, with AC and VC. Note that this is distinct from task connectivity analysis methods such as general functional connectivity (Elliott et al., 2019) in that, rather than exploring connectivity after removing task effects, we aimed instead to identify shared patterns of task responsiveness (coactivation). This was done to capitalize on shared variance (connectivity) between sensory cortex and thalamic nuclei across volumes within a task condition, rather than merely identifying thalamic voxels that activate to task. That is, using only a task contrast [Auditory – Visual] would only pick up on differences driven by the task condition, while the coactivation method employed can be driven by these differences in addition to functional connectivity to sensory cortex that is detectable within each fMRI volume acquired within each condition.

Within each TSR (left and right MGN-TSR and LGN-TSR), coactivation between each voxel's time series and activation in AC and VC (see section **2.8.4**) was estimated using partial correlations, resulting in AC and VC coactivation maps. Note that this produces separate AC and VC coactivation maps for each TSR-MGN and each TSR-LGN search region. Partial correlations included nuisance regressors for average WM, CSF, gray matter signal, local WM (see section **2.8.4**), and a regressor for the second and third image of each cluster.

AC and VC coactivation maps were then thresholded within each TSR to select the highest-ranking voxels (i.e., voxels with the greatest Pearson correlations). TSR-MGN and TSR-LGN upper percentile thresholds were determined separately for each participant, based on the average number of voxels comprising each TSR-MGN and TSR-LGN across hemispheres. The upper percentile threshold for TSR-MGN

coactivation maps was 32 divided by the average number of voxels, and the upper percentile threshold for TSR-LGN coactivation maps was 20 divided by the average number of TSR-LGN voxels. These parameter values are arbitrary, and were selected in order to produce reasonably sized and shaped fROIs, with a stricter threshold in the larger TSR-LGN to accommodate overall greater LGN-VC observed coactivation values. Any voxels remaining in both AC and VC coactivation maps of any TSR after thresholding were then removed from both, in order to improve the specificity of resulting fROIs for sensory modality. The largest contiguous cluster remaining within each hemi-thalamus's TSR-MGN-AC coactivation map, and TSR-LGN-VC coactivation map, were then identified as MGN and LGN, respectively.

Each MGN and LGN fROI was evaluated by multiple members of the study team (J.C.W., P.N.T., and Z.J.Z., and J.X.V.S.) by overlaying them over each participant's high-resolution T1w anatomical images and temporally averaged BOLD TL task EPIs. If issues were noted by any reviewer, they were examined by two members of the study team (J.C.W. and J.X.V.S.) and a consensus was reached. We excluded fROIs that were considered to be anatomically implausible (e.g., an LGN that is either inferior or medial to MGN, or excessive asymmetry between left and right hemispheric MGN or LGN fROIs); data collected from participants with any fROI that failed this quality check (QC) procedure were excluded from further analyses.

2.9 Resting-State Data Analysis

2.9.1 Overview

After localization using the sensory TL task, functional connectivity from MGN and LGN fROIs was evaluated in resting state data obtained from the same participants.

Specificity for connectivity with auditory and visual regions was determined by comparing connectivity between primary AC and VC ROIs (obtained independently of the TL task), and compared with connectivity from alternative MGN and LGN ROIs derived from a standardized atlas, the WFU PickAtlas Toolbox (Maldjian et al., 2004; Maldjian et al., 2003), and two thalamic segmentations using T1w images, the FreeSurfer thalamic nuclei segmentation (Iglesias et al., 2018; Su et al., 2019) and the Thalamus Optimized Multi Atlas Segmentation (THOMAS) segmentation (Iglesias et al., 2018; Su et al., 2019) (see section **2.9.2,** below). We then performed whole-brain seed connectivity analyses to determine functional relationships between signals within TL MGN and LGN fROIs, as well as the differences between functional connectivity maps derived from TL ROIs and those alternative ROIs obtained from the aforementioned atlas and T1w segmentations (Iglesias et al., 2018; Maldjian et al., 2004; Maldjian et al., 2003; Su et al., 2019).

2.9.2 *A Priori* Regions of Interest

ROIs for primary AC and primary VC were obtained from the FreeSurfer Desikan-Killiany segmentation atlas (Desikan et al., 2006; Fischl, 2012; Fischl et al., 2004) output by the HCP MPP (*Atlas_wmparc.2.nii*.gz). AC was created from the transverse temporal gyrus parcel (#1034 and #2034), dilated by one voxel in 3D. The VC mask was created from the pericalcarine gray matter parcels (#1021 and #2021), 3D dilating once, removing any voxels not considered to be in gray matter, and then 3D dilating two more times. These ROIs are shown in **Figure S2.** As a benchmark for the potential for bias in RSFC analysis that would be produced by excessive overlap between primary AC and primary VC ROIs described here and the fROIs derived from

the TL task, we additionally calculated the Dice-Sørensen similarity coefficient (Dice, 1945; Serrano-Sosa et al., 2021) for each participant's TL fROI and *a priori* anatomical ROI, bilaterally, in AC and VC separately.

TL MGN and LGN fROIs were obtained from the thalamic localizer task as described above (see section **2.8.5**). An alternative atlas-based set of left and right MGN and LGN ROIs were obtained from the WFU PickAtlas Toolbox (Maldjian et al., 2004; Maldjian et al., 2003); alternative T1w-segmentation based MGN and LGN ROIs for comparison to the thalamic localizer ROIs developed here were obtained from the FreeSurfer thalamic nuclei segmentation (Iglesias et al., 2018) and the Thalamus Optimized Multi Atlas Segmentation (THOMAS) segmentation (Su et al., 2019), shown in **Figure S3.**

2.9.3 Resting-State Functional Connectivity Analysis

For each run, time series were extracted for each ROI (including fROIs) by spatially averaging unsmoothed volumetric resting-state data within ROI voxels. MGN-AC connectivity was estimated by calculating pairwise Pearson's partial correlations between left MGN and left AC, left MGN and right AC, right MGN and left AC, and right MGN and right AC; these four values were then averaged within each run to create a single run-level MGN-AC connectivity estimate. Both ipsilateral and contralateral connectivity was evaluated in order to account for bilateral processing of sensory stimuli and commissural interhemispheric communication between sensory cortices (Bamiou et al., 2007; Chen et al., 2018; Engel et al., 1991; Ito et al., 2016; Jones, 2007; Lee, 2013; Lee & Winer, 2008; Ramachandra et al., 2020; van der Knaap & van der Ham, 2011), as well as to maximize power. This process was then repeated to additionally calculate

MGN-VC, LGN-AC, and LGN-VC connectivity for each run. This procedure was performed for MGN and LGN fROIs obtained from the sensory TL task, as well as the three alternative ROIs (WFU PickAtlas, FreeSurfer, and THOMAS). Differences between MGN-AC and LGN-VC connectivity estimates produced using TL fROIs and those produced using these alternative ROIs were then estimated for each participant.

Volumetric whole-brain seed connectivity images for each hemisphere's MGN and LGN ROIs were calculated using Pearson's partial correlations between each seed time series and each voxel in 4mm full-width-half-maximum smoothed resting-state images. Connectivity for left and right MGN and LGN TL fROIs was estimated separately, and the two connectivity maps for each geniculi pair were averaged together to produce a single image of bilateral MGN connectivity and a single image of bilateral LGN connectivity. This was repeated for alternative MGN and LGN ROIs generated from WFU PickAtlas, FreeSurfer thalamic segmentation, and THOMAS segmentation. To compare seed connectivity maps derived from TL MGN and LGN fROIs with those derived from each of their three alternatives, six seed connectivity difference images were then calculated for each participant: 1) TL MGN minus WFU MGN, 2) TL MGN minus FreeSurfer MGN, 3) TL MGN minus THOMAS MGN, 4) TL LGN minus WFU LGN, 5) TL LGN minus FreeSurfer LGN, and 6) TL LGN minus THOMAS LGN.

All Pearson's partial correlations were calculated using the following nuisance parameters: band-pass filtered MPs (using the same 0.009-0.08 Hz band-pass filter that was applied to the RS time series), the squares of the band-pass filtered MPs, the derivatives of the band-pass filtered MPs, the squares of the derivatives of the band-pass filtered MPs, the white matter signal and its derivative, and the CSF signal and its

derivative.

2.9.4 Multi-Site Harmonization (ComBat)

ROI pair correlations and seed connectivity images were harmonized across SBU and NYSPI for site and scanner effects using ComBat (Fortin et al., 2018; Fortin et al., 2017; Johnson et al., 2007; Yu et al., 2018) (https://github.com/Jfortin1/ComBatHarmonization/) in MATLAB, using non-parametric adjustments and including demographic covariates. Demographic covariates were included in order to preserve biological variability in the sample while removing the variability associated with sites/scanners. Included covariates included age, gender, handedness, race, ethnicity, and parental socioeconomic status. PANSS Positive Scale, Negative Scale, and General Scale assessment scores were also included, to retain potential variability in auditory and visual perception, as well as other aspects of cognition and affect that might be associated with these measures.

Three participants were missing data for parental socioeconomic status and four participants were missing data for Positive and Negative Syndrome Scale assessments. Missing data were estimated in the full sample of participants who completed the study using SPSS Statistics (Version 29.0.0.0, Build 241, International Business Machines Corporation, Armonk, NY) as the aggregate median of 1,000 imputations, each with a maximum of 100 Markov chain Monte Carlo iterations, using linear regression models for scale variables and two-way interactions among categorical predictors. Singularity tolerance was set to 10^{-12}; maximum case draws and maximum parameter draws were both set to 1,000. Missing data estimates determined via multiple imputation were only used as covariates in the ComBat harmonization procedure, and not in any other

analyses.

2.10 Statistical Analysis

2.10.1 Thalamic Localizer fROIs

As an exploratory analysis, significance was assessed for group-wide interhemispheric differences in TL-derived LGN and MGN fROI sizes using two-tailed Mann–Whitney–Wilcoxon rank-sum tests (Gibbons & Chakraborti, 2021; Hollander et al., 2014). Relationships between fROI size and connectivity with sensory cortex were then assessed, in order to determine whether differences in intrinsic functional connectivity that are observable in task coactivation maps could be systematically driving differences in the sizes of obtained LGN and MGN fROIs, or, conversely, whether differences in fROI sizes could be significantly driving estimates of measured connectivity with sensory cortex. Relationships between fROI sizes and MGN-AC connectivity were assessed using Kendall rank correlation coefficients (tau-b, two-tailed; Kendall, 1990; van Doorn et al., 2021).

2.10.2. ROI Pair Correlation RSFC Analyses

The selectivity of time series extracted from TL MGN and LGN fROIs was evaluated using MGN-AC, MGN-VC, LGN-AC, and LGN-VC connectivity estimates. Using one-tailed paired t-tests, the following relationships were assessed, corrected for false discovery rate (Benjamini & Hochberg, 1995): 1) MGN selectivity for AC over VC (MGN-AC > MGN-VC), 2) AC selectivity for MGN over LGN (MGN-AC > LGN-AC), 3) LGN selectivity for VC over AC (LGN-VC > LGN-AC), and VC selectivity for LGN over MGN (LGN-VC > MGN-VC). One-tailed tests were used because the conclusion drawn from a non-significant result would not differ materially from the conclusion drawn from a

significant two-tailed result in the unexpected direction; in both cases we would conclude that the TL task has failed to properly localize the appropriate thalamic nucleus.

Connectivity between TL fROIs and their appropriate sensory cortex (i.e., MGN-AC connectivity and LGN-VC connectivity) was then benchmarked against connectivity estimates calculated using alternative ROIs from WFU PickAtlas, the FreeSurfer thalamic nuclei segmentation, and the THOMAS segmentation, with the significance of differences assessed using two-tailed, paired t-tests.

2.10.3 Seed Connectivity RSFC Analyses

Whole-brain TL MGN and LGN seed connectivity was assessed for significance using Permutation Analysis of Linear Models (PALM; Alberton et al., 2020; Winkler, Ridgway, et al., 2016; Winkler et al., 2014; Winkler, Webster, et al., 2016; Winkler et al., 2015), with a design matrix consisting of a single column of all 1s, using 10,000 sign-flips, built-in family-wise error rate correction (Holmes et al., 1996), and threshold-free cluster enhancement (TFCE; Smith & Nichols, 2009). All hypothesis testing was two-tailed (bi-sided), performed using two one-directional contrasts followed by multiple testing correction over contrasts (Alberton et al., 2020). This was repeated without TFCE as well, in order to improve the specificity of seed correlation results (at the expense of power). Exploratory analyses in PALM analyses were then conducted identically for difference images comparing seed connectivity between TL MGN and LGN fROIs, and those MGN and LGN ROIs obtained from WFU PickAtlas, FreeSurfer, and THOMAS. T-statistic maps obtained from PALM were thresholded at $\alpha = 0.05$ after correction for family-wise error rate and over contrasts.

3. Results

3.1 Sensory Thalamic Localizer Auditory and Visual Thalamic fROIs (MGN and LGN)

A total of 52 participants (NYSPI n = 30; SBU n = 22) completed at least 2 runs each of the sensory TL and RS data. After evaluation of TL MGN and LGN fROIs, data from 47 participants (26 NYSPI; 21 SBU) were retained for subsequent analysis; fROIs that failed the QC procedure are shown in **Figure S4.** Sample demographics and clinical assessment data before and after exclusions for TL fROI failures are shown in **Table 1.**

Table 1. Demographic and clinical characteristics of study participants

All Study Completers			
Participant Characteristic	**Full Sample (NYSPI+SBU, N = 52)**	**NYSPI (n = 30)**	**SBU (n = 22)**
Age, Years (SD)	30.5 (10.0)	32.2 (9.5)	28.2 (10.5)
Gender, Female (%)	17 (32.7%)	9 (30.0%)	8 (36.4%)
Ethnicity, Hispanic (%)	14 (26.9%)	8 (26.7%)	6 (27.3%)
Race			
Caucasian (%)	17 (32.7%)	9 (30.0%)	8 (36.4%)
African American (%)	21 (40.4%)	13 (43.3%)	8 (36.4%)
Asian (%)	5 (9.6%)	3 (10.0%)	2 (9.1%)
Other (%)	7 (13.5%)	5 (16.7%)	2 (9.1%)
More than one race (%)	2 (3.8%)	0 (0.0%)	2 (9.1%)
Handedness[a]			
Left (%)	2 (3.8%)	1 (3.3%)	1 (4.5%)
Right (%)	48 (92.3%)	29 (96.7%)	19 (86.4%)
Ambidextrous (%)	2 (3.8%)	0 (0.0%)	2 (9.1%)
Smoker[b,c] (%)	3 (5.8%)	3 (10.0%)	0 (0.0%)
Parental SES[d,e] (SD)	44.2 (11.4)	44.4 (11.2)	44.0 (11.8)
PANSS[f] Total (SD)	35.1 (6.9)	32.8 (4.6)	37.7 (8.2)
PANSS[f] General (SD)	18.4 (3.8)	16.2 (3.9)	20.1 (4.5)
PANSS[f] Positive (SD)	7.4 (0.9)	6.9 (1.5)	7.7 (1.2)
PANSS[f] Negative (SD)	9.3 (3.3)	8.8 (2.7)	9.9 (3.8)
Passed Thalamic Localizer fROI QC			
Participant Characteristic	**Full Sample (NYSPI+SBU, N = 47)**	**NYSPI (n = 26)**	**SBU (n = 21)**
Age, Years (SD)	39.9 (9.9)	31.5 (9.1)	28.1 (10.6)
Gender, Female (%)	15 (31.9%)	7 (26.9%)	8 (38.1%)
Ethnicity, Hispanic (%)	14 (29.8%)	8 (30.8%)	6 (28.6%)
Race			
Caucasian (%)	15 (31.9%)	7 (26.9%)	8 (38.1%)
African American (%)	18 (38.3%)	11 (42.3%)	7 (33.3%)
Asian (%)	5 (10.6%)	3 (11.5%)	2 (9.5%)
Other (%)	7 (14.9%)	5 (19.2%)	2 (9.5%)
More than one race (%)	2 (4.3%)	0 (0.0%)	2 (9.5%)
Handedness[a]			
Left (%)	2 (4.3%)	1 (3.8%)	1 (4.8%)
Right (%)	43 (91.5%)	25 (96.2%)	18 (85.7%)

Ambidextrous (%)	2 (4.3%)	0 (0.0%)	2 (9.5%)
Smoker[b] (%)	3 (6.4%)	3 (11.5%)	3 (0.0%)
Parental SES[d,e] (SD)	43.5 (11.6)	43.2 (11.4)	43.8 (11.8)
PANSS Total[f] (SD)	35.4 (7.1)	32.9 (4.8)	38.0 (8.3)
PANSS General[f] (SD)	18.6 (4.0)	17.0 (2.5)	20.2 (4.6)
PANSS Positive[f] (SD)	7.5 (0.9)	7.2 (0.5)	7.8 (1.2)
PANSS Negative[f] (SD)	9.3 (3.3)	8.7 (2.6)	10.0 (3.9)
RSFC Analysis Sample (Passed TL fROI QC + RS Motion Denoising)			
Participant Characteristic	**Full Sample (NYSPI+SBU, N = 42)**	**NYSPI (n = 23)**	**SBU (n = 19)**
Age, Years (SD)	29.6 (9.9)	30.6 (8.8)	28.4 (11.3)
Gender, Female (%)	14 (33.3%)	6 (26.1%)	8 (42.1%)
Ethnicity, Hispanic (%)	12 (28.6%)	6 (26.1%)	6 (31.6%)
Race			
Caucasian (%)	15 (35.7%)	7 (30.4%)	8 (42.1%)
African American (%)	15 (35.7%)	10 (43.5%)	5 (26.3%)
Asian (%)	4 (9.5%)	2 (8.7%)	2 (10.5%)
Other (%)	6 (14.3%)	4 (17.4%)	2 (10.5%)
More than one race (%)	2 (4.8%)	0 (0.0%)	2 (10.5%)
Handedness[a]			
Left (%)	2 (4.8%)	1 (4.3%)	1 (5.3%)
Right (%)	39 (92.3%)	22 (95.7%)	17 (89.5%)
Ambidextrous (%)	1 (2.4%)	0 (0.0%)	1 (5.3%)
Smoker[b] (%)	3 (7.1%)	3 (13.0%)	0 (0.0%)
Parental SES[c,g] (SD)	43.7 (11.7)	43.8 (11.4)	43.6 (12.4)
PANSS Total[h] (SD)	34.9 (6.7)	31.9 (2.4)	37.8 (8.3)
PANSS General[h] (SD)	18.2 (3.7)	15.8 (3.7)	19.9 (4.8)
PANSS Positive[h] (SD)	7.4 (1.0)	6.7 (1.6)	7.8 (1.2)
PANSS Negative[h] (SD)	9.2 (3.2)	8.3 (2.1)	10.1 (3.9)

[a]Handedness was reported using the Edinburgh Handedness Inventory.
[b]Smoking status defined as current daily nicotine use.
[c]Smoking status data were unavailable for 1 NYSPI participant (data excluded after Thalamic Localizer QC).
[d]Mean Parental SES was reported using the Hollingshead Four Factor Index Scale of Socioeconomic Status scale.
[e]Mean Parental SES data were unavailable for 3 participants (2 NYSPI and 1 SBU).
[f]PANSS data were unavailable for 4 NYSPI participants.
[g]Mean Parental SES data were unavailable for 1 NYSPI participant.
[h]PANSS data were unavailable for 4 NYSPI participants.

Abbreviations: fROI: functionally-defined region of interest; NYSPI: New York State Psychiatric Institute; PANSS: Positive and Negative Syndrome Scale; QC: quality check; RS: resting-state; RSFC: resting-state functional connectivity; SBU: Stony Brook University; SD: standard deviation; SES: socioeconomic status.

Group-wide probability density maps and corresponding violin plots of TL fROI sizes across participants are shown in **Figure 2** for left MGN **(Figure 2A-B)**, right MGN **(Figure 2C-D)**, left LGN **(Figure 2E-F)**, and right LGN **(Figure 2G-H).** Median left MGN and right MGN sizes were both 42 voxels, median left LGN size was 46 voxels, and median right LGN size was 50 voxels. LGN size was significant greater in the right than left hemisphere ($p = 5.68 \times 10^{-4}$), consistent with a recent finding using 7 Tesla structural quantitative MR imaging (Muller-Axt et al., 2021), but the interhemispheric difference in MGN size was not ($p = 0.256$). For visualization, probability density maps

were thresholded (binarized) at 50% of the dataset, displayed together in **Figure 3.**

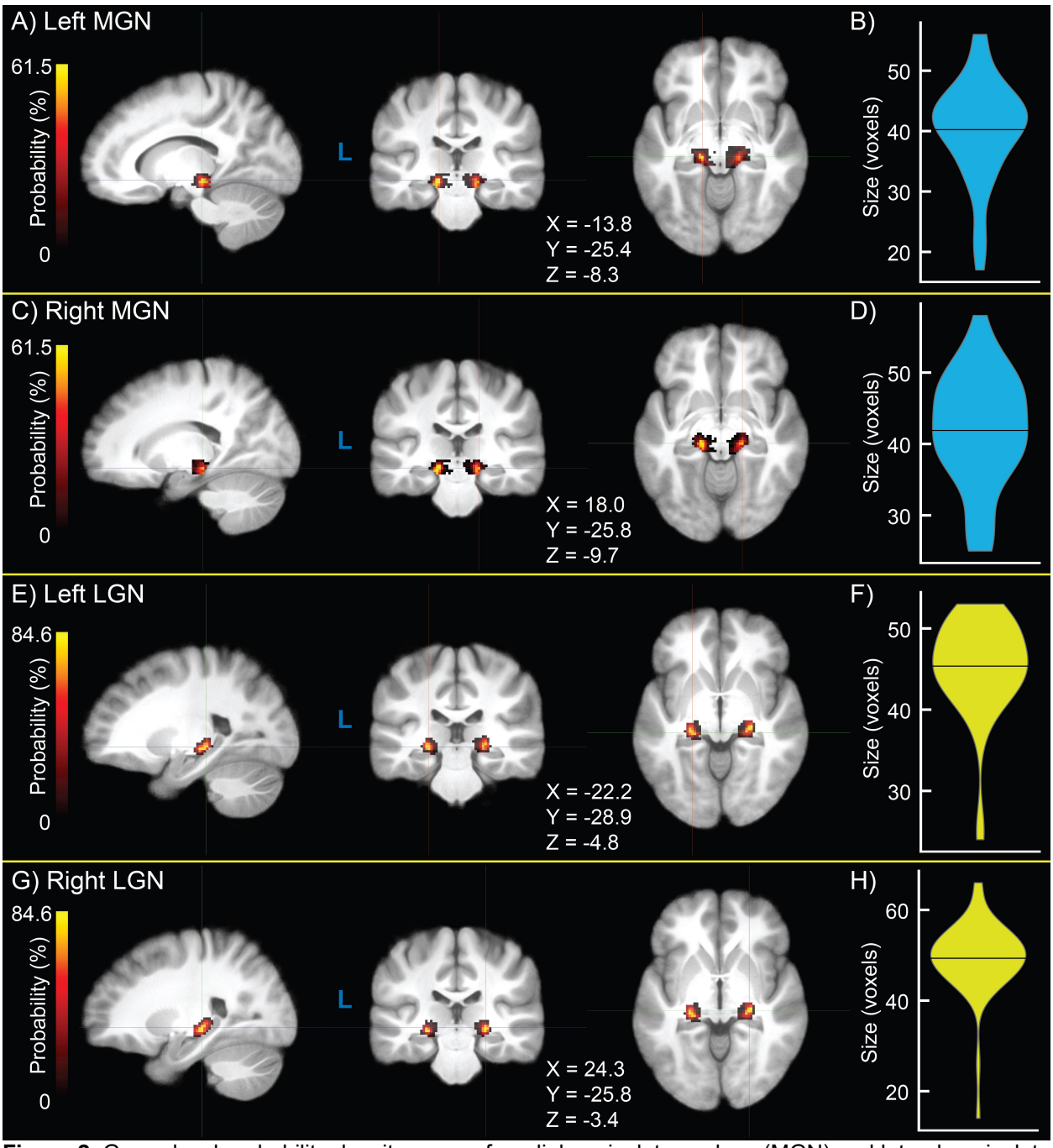

Figure 2. Group-level probability density maps of medial geniculate nucleus (MGN) and lateral geniculate nucleus (LGN) functionally-defined regions of interest (fROIs) obtained from the sensory thalamic localizer (TL) task **(A,C,E,G)** and violin plots of ROI size **(B,D,F,H)** for left MGN **(A,B)**, right MGN **(C,D)**, left LGN **(E,F)**, and right LGN **(G,H)**. Crosshair coordinates for each view are displayed with each set of images.

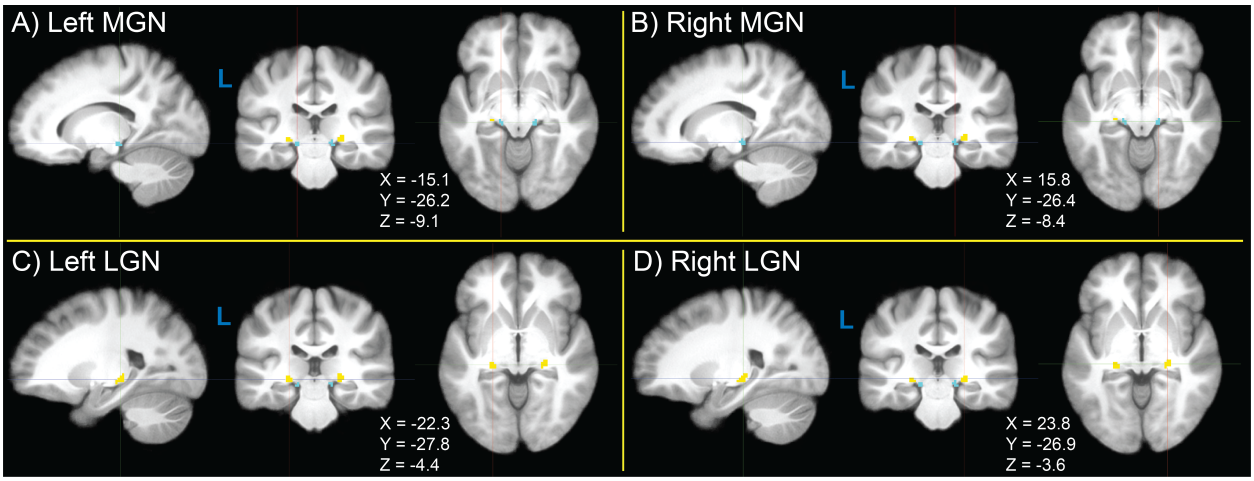

Figure 3. Thresholded (binarized) group-level probability density maps of left and right medial geniculate nucleus (MGN, blue) and lateral geniculate nucleus (LGN, yellow) functionally-defined regions of interest (fROIs) obtained from the sensory thalamic localizer (TL) task. Probability density maps for MGN and LGN were binarized by thresholding at 50% of participants. Image views and crosshairs are centered on the centroid of each fROI in Montreal Neurological Institute (MNI) 152 non-linear 6th-generation (MNI152NLin6), with crosshair coordinates shown for each set of images.

3.2 Resting-State Functional Connectivity Validation of Thalamic Localizer fROIs

Five participants (2 SBU, 3 NYSPI) were excluded from resting-state functional connectivity (RSFC) analyses due to insufficient data remaining after volume censoring, due to excessive participant motion. Descriptive statistics for the final RSFC analysis sample are shown in **Table 1.** An exploratory analysis assessing the association between the size of each hemisphere's MGN and LGN size in each participant and connectivity with sensory cortex (AC and VC, respectively) using Kendall's rank correlation coefficient are shown in **Table S1** (all $p > 0.05$).

Connectivity measured between MGN and LGN fROIs obtained from TL task analysis and AC and VC ROIs obtained from the FreeSurfer atlas (*Atlas_wmparc.2.nii.gz*) is shown in **Figure 4A.** Specificity measurements for MGN and LGN fROIs and their significance are shown in **Figure 4B** (all $p < 0.05$). Dice-Sørensen similarity coefficients between FreeSurfer-derived primary AC and primary VC ROIs and TL-derived AC and VC fROIs used as connectivity seeds for identifying MGN and LGN

fROIs were 0.0533 and 0.115, respectively, indicating minimal bias in these analyses.

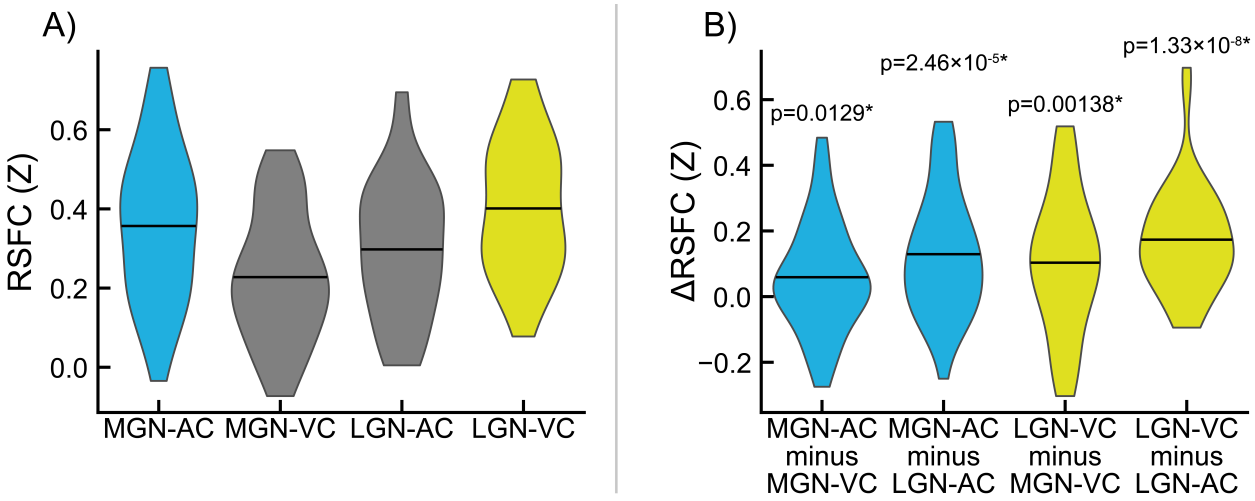

Figure 4. Evaluation of medial geniculate nucleus (MGN) and lateral geniculate nucleus (LGN) functionally-defined regions of interest (fROIs) obtained from the sensory thalamic localizer (TL) task. Pairwise resting-state function connectivity (RSFC) was evaluated between TL-derived geniculi and standard auditory cortex (AC) and visual cortex (VC) ROIs derived from the FreeSurfer atlas (*f*). **A)** Connectivity between MGN and AC (MGN-AC), MGN and VC (MGN-VC), LGN and AC (LGN-AC), and LGN and VC (LGN-VC). **B)** Selectivity of MGN and LGN ROIs for AC and VC, respectively, measured as within-participant differences in the RSFC values shown in panel A. MGN-AC minus MGN-VC quantifies MGN selectivity for AC over VC; MGN-AC minus LGN-AC quantifies AC selectivity for MGN over LGN. Likewise, LGN-VC minus MGN-VC quantifies VC selectivity for MGN over LGN, and LGN-VC minus LGN-AC quantifies LGN selectivity for VC over AC. P-values for significance of sample-wide mean difference are shown; asterisks (*) denote significance after false discovery rate correction (α = 0.05, one-tailed, one-sample t-test).

Whole-brain seed connectivity T-statistic maps are shown for TL MGN and LGN seed correlations, two-sided, thresholded at α = 0.05, and family-wise error rate corrected in **Figure S5.** Broadly distributed whole-brain connectivity is apparent in analyses using TFCE **(Figure S5A-B)**, with increased specificity apparent in voxel-wise (no TFCE) analyses **(Figure S5C-D).** In both images, significant connectivity is visible between MGN and AC, and between LGN and VC.

3.3 Resting-State Functional Connectivity Benchmarking of Thalamic Localizer fROIs

MGN-AC connectivity from MGN fROIs derived from the TL task are shown alongside MGN-AC connectivity from MGN ROIs derived from the WFU atlas (Maldjian

et al., 2004; Maldjian et al., 2003), the FreeSurfer segmentation (Iglesias et al., 2018), and THOMAS segmentation (Su et al., 2019) in **Figure 5A**, and differences between MGN-AC connectivity estimates from TL fROIs and each of the other ROIs are shown in **Figure 5C**, along with P values for these connectivity differences. Similarly, LGN-VC

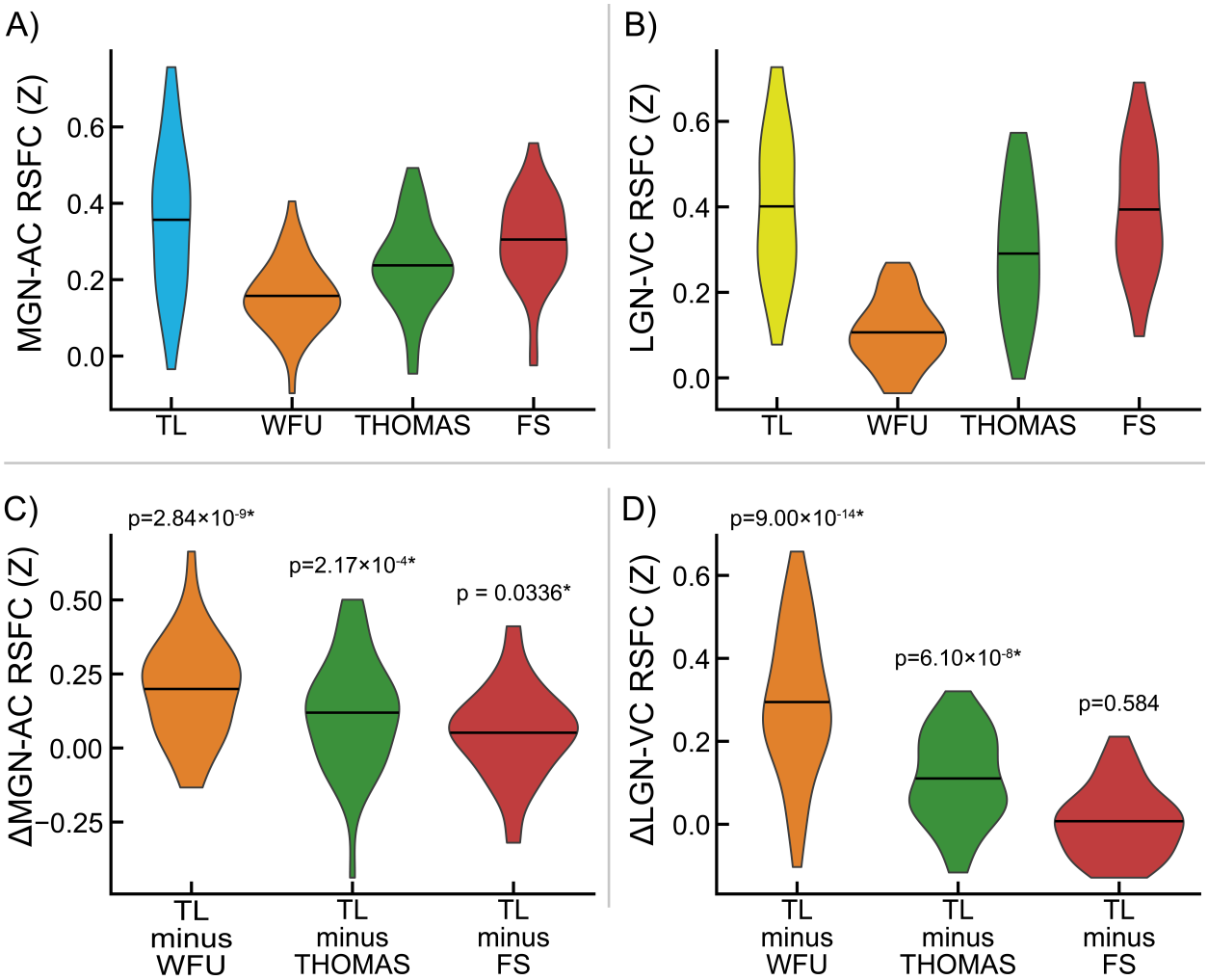

Figure 5. Benchmarking of medial geniculate nucleus (MGN) and lateral geniculate nucleus (LGN) functionally-defined regions of interest (fROIs) obtained from the sensory thalamic localizer (TL) task through resting-state functional connectivity (RSFC) with auditory cortex (AC) and visual cortex (VC) ROIs, respectively. AC and VC regions of interest (ROIs) were obtained from the FreeSurfer (FS) Desikan-Killiany atlas (*Atlas_wmparc.2.nii.gz*). MGN and LGN derived from the TL task are evaluated relative to those derived from 1) MNI space atlas ROIs from the Wake Forest University (WFU) PickAtlas, 2) THOMAS segmentation applied to each subject's T1w image, and 3) the FreeSurfer thalamic segmentation applied to each subject's T1w. Panel **A** shows MGN-AC RSFC using the TL MGN ROI alongside the three named alternatives; panel **B** shows the within-participant differences between MGN-AC connectivity from the TL-derived MGNs and the three alternatives (i.e., differences between TL and other values in panel A). Likewise, panel **C** shows LGN-VC RSFC using the TL LGN ROI alongside alternatives derived from WFU, THOMAS, and FS; panel **D** shows the within-participant differences between TL connectivity and the three alternatives shown in panel **C**. P-values for significance of sample-wide mean difference are shown; asterisks (*) denote significance ($\alpha < 0.05$, two-tailed, one-sample t-test).

connectivity estimates derived from TL task LGN fROIs are shown in **Figure 5B**, alongside LGN-VC connectivity estimates derived using WFU, THOMAS, and LGN ROIs. Differences in LGN-VC connectivity observed between TL LGN fROIs and the three alternatives are shown in **Figure 5D.** MGN-AC connectivity was significantly greater when using the TL task ROIs relative to the three alternatives (vs. WFU, $p = 2.84\times10^{-9}$; vs. THOMAS, $p = 2.17\times10^{-4}$; vs. FreeSurfer, $p = 3.36\times10^{-2}$). TL LGN-VC connectivity was observed to be greater relative to the three alternatives, significantly versus WFU ($p = 9.00\times10^{-14}$) and THOMAS ($p = 6.10\times10^{-8}$), but not significantly versus FreeSurfer ($p = 0.584$).

Exploratory analyses assessing for differences in seed connectivity between TL MGN and LGN fROIs, and the three evaluated alternatives (WFU, THOMAS, and FreeSurfer), are shown in **Figure 6**. Significant whole-brain increases in connectivity brain are visible relative to WFU ROIs **(Figure 6, panels A and D).** TL MGN fROIs show increased connectivity with areas of primary AC and superior temporal gyrus relative to all alternative ROIs **(Figure 6A-C).** Similarly, TL LGN fROIs show increased connectivity compared to the WFU and THOMAS ROIs across the brain, with particularly increased connectivity with regions of primary VC around the calcarine sulcus **(Figure 6D-E).** No significant differences in TL LGN seed connectivity and FreeSurfer seed connectivity were found after correction for family-wise error rate.

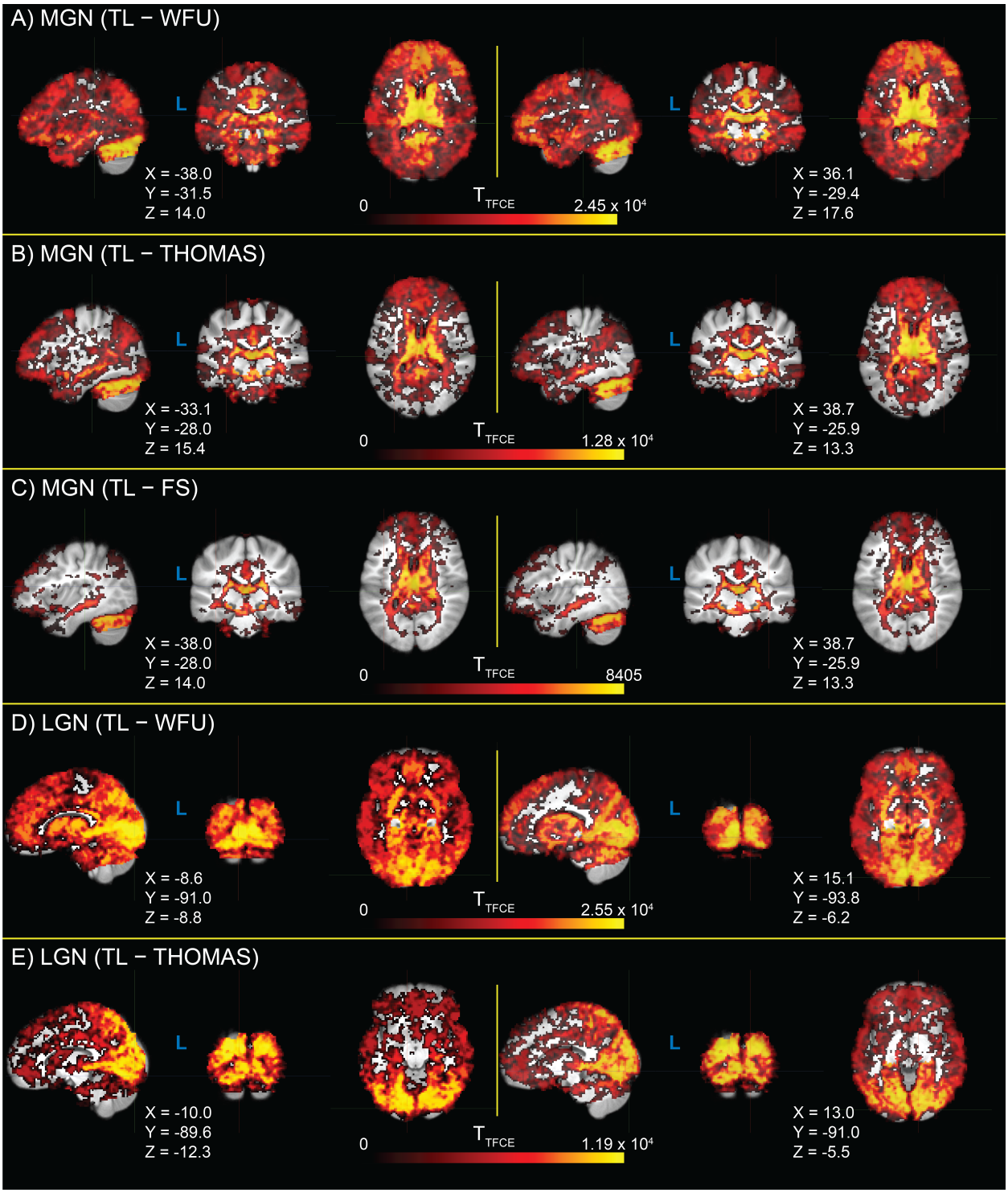

Figure 6. Whole-brain T-statistic maps for differences in seed connectivity between thalamic localizer (TL) derived medial geniculate nucleus (MGN) and lateral geniculate nucleus (LGN) functionally-defined regions of interest (fROIs), relative to seed connectivity calculated from three alternative regions of interest (ROIs): Wake Forest University PickAtlas (WFU), the Thalamus Optimized Multi Atlas Segmentation (THOMAS), and the FreeSurfer thalamic nuclei segmentation (FS). T-statistics are thresholded at α = 0.05 (two-tailed, family-wise error rate corrected). Image views are centered on either auditory cortex (panels **A-C**) or visual cortex (panels **D** and **E**) of each hemisphere, with crosshair coordinates for each view shown. A panel for LGN TL − FS T-statistics is not shown, as there were no significant voxels.

4. Discussion

Here, we detail a sensory thalamic localizer (TL) fMRI task (design shown in **Figure 1**) capable of localizing auditory and visual thalamic nuclei in individual human participants (shown in **Figure 2** and **Figure 3)**. Building off of past work (Chen et al., 1998; Denison et al., 2014; Jiang et al., 2013; Kastner et al., 2004), in which localizer tasks were utilized in order to identify either medial or lateral geniculate nuclei, here we show identification of both MGN and LGN through the use of a single task. Additionally, this task provides estimates of these thalamic nuclei in 16 minutes 12 seconds total, across 4 runs (of 3 minutes 46 seconds each), which is substantially less time than in prior work. For example, a single set of auditory thalamic fROIs was acquired in 32 minutes, across 6 runs (of 5 minutes and 20 seconds each) (Jiang et al., 2013). This is likely at least partially due to improvements in data acquisition: data here were acquired using 3 Tesla MR scanners, using a head coil with 32 or more channels (i.e., 32-channel at NYSPI and 48 head coil channels in the 64-channel head-and-neck coil at SBU), a high-resolution simultaneous-multi-slice (multiband) acquisition sequence (Moeller et al., 2010), and clustered-sparse temporal acquisition (Schmidt et al., 2008; Yang et al., 2000; Zaehle et al., 2007) of 3 volumes per cluster.

Additionally, improvements in the ability to resolve the location of auditory and visual thalamic fROIs is potentially enabled in part due to novel elements of the task design, in which a contrast between auditory and visual stimuli was used to robustly detect responsive regions around auditory and visual cortices in each subject, and use these task time series to find thalamic voxels (within specified search regions) that are responsive to either, but not to both. The contrast produced by alternating task

conditions serves as a sensory control condition, in which circuits involved in the conscious perception of stimulation generally are engaged in both conditions. Furthermore, this design increases the specificity of obtained thalamic nuclei: auditory and visual thalamic fROIs are optimized to represent regions specific to their sensory modality, and not general features of perception or cognition. This may be critical in studies that aim to relate human perceptual abnormalities to dysfunction in circuits specifically associated with either auditory or visual processing. We validated this specificity using resting-state functional connectivity (RSFC) data **(Figure 4)** collected from the same participants.

Finally, we compared fROIs obtained from the TL task to three alternative sources of thalamic ROIs **(Figure 5)**: an atlas-based ROI from the Wake Forest University PickAtlas Toolbox (Maldjian et al., 2004; Maldjian et al., 2003), the Thalamus Optimized Multi Atlas Segmentation (THOMAS; Su et al., 2019) and the FreeSurfer thalamic nuclei segmentation (Iglesias et al., 2018). We found significantly greater connectivity with auditory cortex from TL MGN fROIs relative to the evaluated alternatives, and significantly greater connectivity with visual cortex from TL LGN fROIs relative to the WFU and THOMAS ROIs; average connectivity from the FreeSurfer LGN ROI to visual cortex was slightly increased, but not significantly so. This may be due in part to the fact that FreeSurfer MGN ROIs are utilized during TL task analysis as the starting point for building search regions for these fROIs, and may additionally represent that priors for LGN locations in the FreeSurfer segmentation are typically well-placed for detecting BOLD activation from visual thalamus. This pattern is also visible in exploratory whole-brain seed correlation analyses exploring regions showing significant

differences in connectivity from TL MGN and LGN fROIs relative to the three aforementioned alternative ROIs **(Figure 6).**

4.1 Caveats and Limitations

One critical aspect of fROIs derived from the TL task described here is that these fROIs purport to represent the profile of the hemodynamic signature of geniculate nuclei's neural responses during task stimulation as detected in BOLD echo planar images, including the point spread functions of the hemodynamic response and T2* contrast (Parkes et al., 2005; Shmuel et al., 2007; Ugurbil, 2016; Ugurbil et al., 2013; Vu et al., 2017), after pre-processing and post-processing (including spatial smoothing). Thus they may not correspond fully to anatomically expected sizes observed in human tissue post-mortem, or *in vivo* using anatomical (as opposed to functional) imaging techniques (Garcia-Gomar et al., 2019; Muller-Axt et al., 2021; Oishi et al., 2023; Sitek et al., 2019; Tourdias et al., 2014). When using these fROIs in BOLD fMRI data analysis, this could be a substantial advantage, since they may better map onto specific spatial features of the thalamic hemodynamic response and its profile in BOLD images, which can be impacted by imperfectly corrected susceptibility distortions, errors in spatial normalization to MNI template space, and other errors in localization. However, depending on the application, this advantage may be a flaw, and other techniques may prove superior; for example, when attempting to evaluate specific features of individual anatomy that are too fine to be reliably detected with standard whole-brain 3 Tesla BOLD imaging techniques. Likewise, aspects of human perceptual processing that occur at faster timescales than the Nyquist frequency enabled by BOLD fMRI imaging techniques (e.g., 800 ms) are not detectable using fMRI, except through summation into

a slower, aggregate hemodynamic response.

Additionally, TL task-derived fROIs aim to achieve a degree of specificity to sensory modality, which could preclude their use for aspects of perception that involve multisensory integration or context-dependent modulation, including the medial and dorsal subnuclei of the MGN (Lee, 2015; Wepsic, 1966). While this does not appear to be a significant issue given the smoothness of 3T BOLD fMRI, especially after Gaussian smoothing, and the relatively large voxel size of 2 mm (isotropic), this could require modification if adapting this task for more precise mapping of geniculi using higher field strengths or more specialized sequences.

The TL task requires dedicated data acquisition of slightly more than 15 minutes total; this is in addition to standard T1w and T2w sequences, which can be used to obtain ROIs from anatomical segmentations. Future work systematically exploring the impact of scan time on fROI quality is warranted in order to aid in balancing needs for data quality against the feasibility of adding the task to a scan protocol. In this study, task data acquired from 5 of 52 (9.6%) participants did not produce a full set of four valid thalamic fROIs, which may be a concern in studies with limited sample sizes or variable data quality, and the extent to which additional data collection could have reduced this failure rate is unknown. As this study did not include the evaluation of test-retest reliability of fROIs obtained from the sensory TL task, future work should aim to quantify this by obtaining multiple sessions of sensory TL task data for each participant and explore the relationship between reliability measures and scan time.

Finally, the task code is written in Presentation, and the analysis code in MATLAB. These are proprietary software tools that require paid licenses to use. Future

work exploring the adaptation of the task code to utilize free alternatives, such as Python (Python Software Foundation, Wilmington, DE) and PsychoPy (Peirce et al., 2019; Peirce, 2007, 2008), would allow for greater accessibility to researchers. As this software is open-source and released under the GNU General Public License version 3, it may be translated to other platforms and programming languages, as well as extended or adapted for other purposes as desired by the wider research community.

4.2 Conclusion

This work details the development, implementation, validation, and benchmarking of a sensory thalamic localizer (TL) BOLD fMRI task capable of detecting auditory and visual thalamic nuclei in individual participants. Using resting-state functional connectivity analyses, we show that auditory and visual thalamic functionally-defined regions of interest (fROIs) obtained from the sensory TL task are modality specific, and benchmark them against existing atlas- and T1w segmentation-based alternatives. This task produces estimated thalamic medial and lateral geniculate fROIs suitable for resting-state functional connectivity (RSFC) studies and may be added to fMRI acquisition protocols with less than 16 minutes of dedicated additional acquisition time. The TL task, implemented in Presentation, and analysis code, implemented in MATLAB, are both publicly available to the research community.

5 Data and Code Availability

The sensory Thalamic Localizer Presentation task code (Williams et al., 2024) is available from GitHub at https://github.com/CNaP-Lab/Sensory-Thalamic-Localizer and the Neurobehavioral Systems Archives of Neurobehavioral Experiments and Stimuli at http://www.neurobs.com/ex_files/expt_view?id=302. The MATLAB task analysis code

for producing MGN and LGN fROIs from acquired BOLD fMRI task data and Presentation task logs is additionally available from GitHub at https://github.com/CNaP-Lab/Sensory-Thalamic-Localizer. All software associated with this manuscript is released under the GNU General Public License version 3. Note that the sensory Thalamic Localizer task is designed to be deployed on a system with a display refresh rate of 60 Hz. Data acquired from human participants used in the analyses detailed in this manuscript are available upon request from the corresponding author through a formal data sharing agreement.

6 Author Contributions

Conceptualization: G.H., A.A-D., and J.X.V.S.; **Data Curation:** J.C.W., P.N.T., Z.J.Z., E.B.S-F., D.T.P., N.K.H., S.K.A., G.H., and J.X.V.S.; **Formal Analysis:** J.C.W., P.N.T., and J.X.V.S.; **Funding Acquisition:** J.C.W., A.A-D., G.H., and J.X.V.S.; **Investigation:** J.C.W., P.N.T., Z.J.Z., E.B.S-F., D.T.P., N.K.H., S.K.A., A.A-D., G.H., and J.X.V.S.; **Methodology:** J.C.W., P.N.T., G.H., and J.X.V.S.; **Project Administration:** J.C.W., N.K.H., A.A-D., G.H., and J.X.V.S.; **Resources:** A.A-D., G.H., and J.X.V.S.; **Software:** J.C.W., P.N.T., S.K.A., and J.X.V.S.; **Supervision:** N.K.H., A.A-D., G.H., and J.X.V.S.; **Validation:** J.C.W., S.K.A, G.H., and J.X.V.S.; **Visualization:** J.C.W., P.N.T., D.T.P., and J.X.V.S.; **Writing – Original Draft:** J.C.W.; **Writing – Review & Editing:** J.C.W., P.N.T., Z.J.Z., A.A-D., G.H., and J.X.V.S.

7 Funding

Research reported in this publication was supported by the National Institute of Mental Health of the National Institutes of Health (NIH) under award numbers K01MH107763 to J.X.V.S., K23MH101637 to G.H., R01MH109635 to A.A-D., and

F30MH122136 to J.C.W. J.C.W. was also supported by an NIH Research Supplement to Promote Diversity in Health-Related Research (3R01MH120293-04S1) and by the Stony Brook University Medical Scientist Training Program (NIH Award No. T32GM008444; Principal Investigator: Dr. Michael A. Frohman). P.N.T. was supported by a Stony Brook University Department of Biomedical Engineering Graduate Assistance in Areas of National Need Fellowship (United States Department of Education Award No. P200A210006; Director: Dr. David Rubenstein) and the Stony Brook University Scholars in Biomedical Sciences Program (NIH Award No. T32GM148331; PI: Dr. Styliani-Anna [Stella] E. Tsirka). The Stony Brook high-performance SeaWulf computing system was supported by National Science Foundation (NSF) Award Nos. 1531492 (PI: Dr. Robert Harrison; co-PI: Dr. Yuefan Deng) and 2215987 (PI: Dr. Robert Harrison; co-PIs: Dr. Yuefan Deng, Dr. Eva Siegmann, and David Cyrille), and matching funds from the Empire State Development's Division of Science, Technology and Innovation (NYSTAR) program contract C210148. Magnetic resonance imaging at Stony Brook University was performed at the Social, Cognitive, and Affective Neuroscience (SCAN) Center, supported by NSF Award No. 0722874 (PI: Dr. Turhan Canli). The content is solely the responsibility of the authors and does not necessarily represent the official views of the NIH, NSF, or NYSTAR.

8 Declaration of Competing Interests

Anissa Abi-Dargham received consulting fees and/or honoraria from Sunovion Pharmaceuticals Inc., Otsuka Pharmaceutical Co., Ltd., Merck & Co., Inc., Neurocrine Biosciences, Inc., F. Hoffmann-La Roche AG, and C.H. Boehringer Sohn AG & Co. KG.

Anissa Abi-Dargham holds stock options in Herophilus, Inc. and in Terran Biosciences, Inc. All other authors declare that they have no known competing financial interests or personal relationships that could have influenced or appear to have influenced the work reported in this paper.

9 Acknowledgements

The authors would like to thank Jaeyop Jeong, Sam R. Luceno, Srineil Nizambad, and Yash Patel for contributions to fMRI data preprocessing, Kelly Bobchin for assistance with data organization, and Tram Ngoc Bao Nguyen for helpful discussions. Computing resources and technical assistance were provided by Stony Brook Medicine Research Computing, with substantial support from Allen Zawada and James Xikis. Access to and technical support for the high-performance SeaWulf computing system was provided by Stony Brook Research Computing and Cyberinfrastructure and the Institute for Advanced Computational Science at Stony Brook University, with notable support from Fırat Coşkun, Daniel Wood, and David Carlson.

References

Alberton, B. A. V., Nichols, T. E., Gamba, H. R., & Winkler, A. M. (2020). Multiple testing correction over contrasts for brain imaging. *Neuroimage*, *216*, 116760. https://doi.org/10.1016/j.neuroimage.2020.116760

Almasabi, F., Janssen, M. L. F., Devos, J., Moerel, M., Schwartze, M., Kotz, S. A., Jahanshahi, A., Temel, Y., & Smit, J. V. (2022). The role of the medial geniculate body of the thalamus in the pathophysiology of tinnitus and implications for treatment. *Brain Res*, *1779*, 147797. https://doi.org/10.1016/j.brainres.2022.147797

American Psychiatric Association. (2000). *Diagnostic and statistical manual of mental disorders : DSM-IV-TR* (4th ed., text revision. ed.). American Psychiatric Association.

American Psychiatric Association. (2013). *Diagnostic and statistical manual of mental disorders : DSM-5* (5th ed.). American Psychiatric Association. https://doi.org/10.1176/appi.books.9780890425596

Andrews, T. J., Halpern, S. D., & Purves, D. (1997). Correlated size variations in human visual cortex, lateral geniculate nucleus, and optic tract. *J Neurosci*, *17*(8), 2859-2868. https://doi.org/10.1523/JNEUROSCI.17-08-02859.1997

Anticevic, A., Cole, M. W., Repovs, G., Murray, J. D., Brumbaugh, M. S., Winkler, A. M., Savic, A., Krystal, J. H., Pearlson, G. D., & Glahn, D. C. (2014). Characterizing thalamo-cortical disturbances in schizophrenia and bipolar illness. *Cereb Cortex*, *24*(12), 3116-3130. https://doi.org/10.1093/cercor/bht165

Anticevic, A., Haut, K., Murray, J. D., Repovs, G., Yang, G. J., Diehl, C., McEwen, S. C.,

Bearden, C. E., Addington, J., Goodyear, B., Cadenhead, K. S., Mirzakhanian, H., Cornblatt, B. A., Olvet, D., Mathalon, D. H., McGlashan, T. H., Perkins, D. O., Belger, A., Seidman, L. J.,…Cannon, T. D. (2015). Association of Thalamic Dysconnectivity and Conversion to Psychosis in Youth and Young Adults at Elevated Clinical Risk. *JAMA Psychiatry*, *72*(9), 882-891. https://doi.org/10.1001/jamapsychiatry.2015.0566

Bamiou, D. E., Sisodiya, S., Musiek, F. E., & Luxon, L. M. (2007). The role of the interhemispheric pathway in hearing. *Brain Res Rev*, *56*(1), 170-182. https://doi.org/10.1016/j.brainresrev.2007.07.003

Bandettini, P. A., Jesmanowicz, A., Van Kylen, J., Birn, R. M., & Hyde, J. S. (1998). Functional MRI of brain activation induced by scanner acoustic noise. *Magn Reson Med*, *39*(3), 410-416. https://doi.org/10.1002/mrm.1910390311

Bartlett, E. L. (2013). The organization and physiology of the auditory thalamus and its role in processing acoustic features important for speech perception. *Brain Lang*, *126*(1), 29-48. https://doi.org/10.1016/j.bandl.2013.03.003

Benjamini, Y., & Hochberg, Y. (1995). Controlling the False Discovery Rate: A Practical and Powerful Approach to Multiple Testing. *Journal of the Royal Statistical Society: Series B (Methodological)*, *57*(1), 289-300. https://doi.org/10.1111/j.2517-6161.1995.tb02031.x

Berman, M. G., Park, J., Gonzalez, R., Polk, T. A., Gehrke, A., Knaffla, S., & Jonides, J. (2010). Evaluating functional localizers: the case of the FFA. *Neuroimage*, *50*(1), 56-71. https://doi.org/10.1016/j.neuroimage.2009.12.024

Brodal, A. (1981). *Neurological anatomy in relation to clinical medicine* (3d ed.). Oxford

University Press. Publisher description http://www.loc.gov/catdir/enhancements/fy0603/80011701-d.html

Carhart, R., & Tillman, T. W. (1966). Northwestern University Auditory Test No. 6. *Audiology*, *5*(2), 83-93. https://doi.org/10.3109/00206096609078425

Chen, W., Kato, T., Zhu, X. H., Strupp, J., Ogawa, S., & Ugurbil, K. (1998). Mapping of lateral geniculate nucleus activation during visual stimulation in human brain using fMRI. *Magn Reson Med*, *39*(1), 89-96. https://doi.org/10.1002/mrm.1910390115

Chen, Z., Kosovicheva, A., Wolfe, B., Cavanagh, P., Gorea, A., & Whitney, D. (2018). Unifying Visual Space Across the Left and Right Hemifields. *Psychol Sci*, *29*(3), 356-369. https://doi.org/10.1177/0956797617735534

Chun, S., Du, F., Westmoreland, J. J., Han, S. B., Wang, Y. D., Eddins, D., Bayazitov, I. T., Devaraju, P., Yu, J., Mellado Lagarde, M. M., Anderson, K., & Zakharenko, S. S. (2017). Thalamic miR-338-3p mediates auditory thalamocortical disruption and its late onset in models of 22q11.2 microdeletion. *Nat Med*, *23*(1), 39-48. https://doi.org/10.1038/nm.4240

Chun, S., Westmoreland, J. J., Bayazitov, I. T., Eddins, D., Pani, A. K., Smeyne, R. J., Yu, J., Blundon, J. A., & Zakharenko, S. S. (2014). Specific disruption of thalamic inputs to the auditory cortex in schizophrenia models. *Science*, *344*(6188), 1178-1182. https://doi.org/10.1126/science.1253895

Denison, R. N., Vu, A. T., Yacoub, E., Feinberg, D. A., & Silver, M. A. (2014). Functional mapping of the magnocellular and parvocellular subdivisions of human LGN. *Neuroimage*, *102 Pt 2*(0 2), 358-369.

https://doi.org/10.1016/j.neuroimage.2014.07.019

Desikan, R. S., Segonne, F., Fischl, B., Quinn, B. T., Dickerson, B. C., Blacker, D., Buckner, R. L., Dale, A. M., Maguire, R. P., Hyman, B. T., Albert, M. S., & Killiany, R. J. (2006). An automated labeling system for subdividing the human cerebral cortex on MRI scans into gyral based regions of interest. *Neuroimage*, *31*(3), 968-980. https://doi.org/10.1016/j.neuroimage.2006.01.021

Dice, L. R. (1945). Measures of the Amount of Ecologic Association Between Species. *Ecology*, *26*(3), 297-302. https://doi.org/https://doi.org/10.2307/1932409

Dodell-Feder, D., Koster-Hale, J., Bedny, M., & Saxe, R. (2011). fMRI item analysis in a theory of mind task. *Neuroimage*, *55*(2), 705-712. https://doi.org/10.1016/j.neuroimage.2010.12.040

Elliott, M. L., Knodt, A. R., Cooke, M., Kim, M. J., Melzer, T. R., Keenan, R., Ireland, D., Ramrakha, S., Poulton, R., Caspi, A., Moffitt, T. E., & Hariri, A. R. (2019). General functional connectivity: Shared features of resting-state and task fMRI drive reliable and heritable individual differences in functional brain networks. *Neuroimage*, *189*, 516-532. https://doi.org/10.1016/j.neuroimage.2019.01.068

Engel, A. K., Konig, P., Kreiter, A. K., & Singer, W. (1991). Interhemispheric synchronization of oscillatory neuronal responses in cat visual cortex. *Science*, *252*(5009), 1177-1179. https://doi.org/10.1126/science.252.5009.1177

Erskine, D., Taylor, J. P., Firbank, M. J., Patterson, L., Onofrj, M., O'Brien, J. T., McKeith, I. G., Attems, J., Thomas, A. J., Morris, C. M., & Khundakar, A. A. (2016). Changes to the lateral geniculate nucleus in Alzheimer's disease but not dementia with Lewy bodies. *Neuropathol Appl Neurobiol*, *42*(4), 366-376.

https://doi.org/10.1111/nan.12249

Fedorenko, E., Hsieh, P. J., Nieto-Castanon, A., Whitfield-Gabrieli, S., & Kanwisher, N. (2010). New method for fMRI investigations of language: defining ROIs functionally in individual subjects. *J Neurophysiol*, *104*(2), 1177-1194. https://doi.org/10.1152/jn.00032.2010

First, M. B., & Gibbon, M. (2004). The Structured Clinical Interview for DSM-IV Axis I Disorders (SCID-I) and the Structured Clinical Interview for DSM-IV Axis II Disorders (SCID-II). In *Comprehensive handbook of psychological assessment, Vol. 2: Personality assessment.* (pp. 134-143). John Wiley & Sons, Inc.

First, M. B., Williams, J. B. W., Karg, R. S., & Spitzer, R. L. (2015). *Structured Clinical Interview for DSM-5 Disorders, Research Version*. American Psychiatric Association Publishing.

Fischl, B. (2012). FreeSurfer. *Neuroimage*, *62*(2), 774-781. https://doi.org/10.1016/j.neuroimage.2012.01.021

Fischl, B., van der Kouwe, A., Destrieux, C., Halgren, E., Segonne, F., Salat, D. H., Busa, E., Seidman, L. J., Goldstein, J., Kennedy, D., Caviness, V., Makris, N., Rosen, B., & Dale, A. M. (2004). Automatically parcellating the human cerebral cortex. *Cereb Cortex*, *14*(1), 11-22. https://doi.org/10.1093/cercor/bhg087

Fortin, J. P., Cullen, N., Sheline, Y. I., Taylor, W. D., Aselcioglu, I., Cook, P. A., Adams, P., Cooper, C., Fava, M., McGrath, P. J., McInnis, M., Phillips, M. L., Trivedi, M. H., Weissman, M. M., & Shinohara, R. T. (2018). Harmonization of cortical thickness measurements across scanners and sites. *Neuroimage*, *167*, 104-120. https://doi.org/10.1016/j.neuroimage.2017.11.024

Fortin, J. P., Parker, D., Tunc, B., Watanabe, T., Elliott, M. A., Ruparel, K., Roalf, D. R., Satterthwaite, T. D., Gur, R. C., Gur, R. E., Schultz, R. T., Verma, R., & Shinohara, R. T. (2017). Harmonization of multi-site diffusion tensor imaging data. *Neuroimage*, *161*, 149-170. https://doi.org/10.1016/j.neuroimage.2017.08.047

Friston, K. J., Ashburner, J., Kiebel, S., Nichols, T., & Penny, W. D. (2007). *Statistical parametric mapping : the analysis of funtional brain images* (First edition. ed.). Elsevier/Academic Press,. https://doi.org/doi.org/10.1016/B978-0-12-372560-8.X5000-1

Friston, K. J., Holmes, A. P., Worsley, K. J., Poline, J. P., Frith, C. D., & Frackowiak, R. S. J. (1994). Statistical parametric maps in functional imaging: A general linear approach [https://doi.org/10.1002/hbm.460020402]. *Human Brain Mapping*, *2*(4), 189-210. https://doi.org/10.1002/hbm.460020402

Friston, K. J., Jezzard, P., & Turner, R. (1994). Analysis of functional MRI time-series [https://doi.org/10.1002/hbm.460010207]. *Human Brain Mapping*, *1*(2), 153-171. https://doi.org/10.1002/hbm.460010207

Garcia-Gomar, M. G., Strong, C., Toschi, N., Singh, K., Rosen, B. R., Wald, L. L., & Bianciardi, M. (2019). In vivo Probabilistic Structural Atlas of the Inferior and Superior Colliculi, Medial and Lateral Geniculate Nuclei and Superior Olivary Complex in Humans Based on 7 Tesla MRI. *Front Neurosci*, *13*, 764. https://doi.org/10.3389/fnins.2019.00764

Gibbons, J. D., & Chakraborti, S. (2021). *Nonparametric statistical inference* (6th edition. ed.). CRC Press.

Gilbert, C. D., & Li, W. (2013). Top-down influences on visual processing. *Nat Rev Neurosci*, *14*(5), 350-363. https://doi.org/10.1038/nrn3476

Giraldo-Chica, M., Hegarty, J. P., 2nd, & Schneider, K. A. (2015). Morphological differences in the lateral geniculate nucleus associated with dyslexia. *Neuroimage Clin*, *7*, 830-836. https://doi.org/10.1016/j.nicl.2015.03.011

Giraldo-Chica, M., Rogers, B. P., Damon, S. M., Landman, B. A., & Woodward, N. D. (2018). Prefrontal-Thalamic Anatomical Connectivity and Executive Cognitive Function in Schizophrenia. *Biol Psychiatry*, *83*(6), 509-517. https://doi.org/10.1016/j.biopsych.2017.09.022

Giraldo-Chica, M., & Schneider, K. A. (2018). Hemispheric asymmetries in the orientation and location of the lateral geniculate nucleus in dyslexia. *Dyslexia*, *24*(2), 197-203. https://doi.org/10.1002/dys.1580

Glasser, M. F., Sotiropoulos, S. N., Wilson, J. A., Coalson, T. S., Fischl, B., Andersson, J. L., Xu, J., Jbabdi, S., Webster, M., Polimeni, J. R., Van Essen, D. C., Jenkinson, M., & Consortium, W. U.-M. H. (2013). The minimal preprocessing pipelines for the Human Connectome Project. *Neuroimage*, *80*, 105-124. https://doi.org/10.1016/j.neuroimage.2013.04.127

Grabner, G., Janke, A. L., Budge, M. M., Smith, D., Pruessner, J., & Collins, D. L. (2006). Symmetric atlasing and model based segmentation: an application to the hippocampus in older adults. *Med Image Comput Comput Assist Interv*, *9*(Pt 2), 58-66. https://doi.org/10.1007/11866763_8

Hess, R. F., Thompson, B., Gole, G., & Mullen, K. T. (2009). Deficient responses from the lateral geniculate nucleus in humans with amblyopia. *Eur J Neurosci*, *29*(5),

1064-1070. https://doi.org/10.1111/j.1460-9568.2009.06650.x

Hollander, M., Wolfe, D. A., & Chicken, E. (2014). *Nonparametric statistical methods* (Third edition / ed.). John Wiley & Sons, Inc.

Hollingshead, A. B. (1975). Four factor index of social status. *Working paper published by the author*.

Holmes, A. P., Blair, R. C., Watson, J. D., & Ford, I. (1996). Nonparametric analysis of statistic images from functional mapping experiments. *J Cereb Blood Flow Metab*, *16*(1), 7-22. https://doi.org/10.1097/00004647-199601000-00002

Horga, G., Schatz, K. C., Abi-Dargham, A., & Peterson, B. S. (2014). Deficits in predictive coding underlie hallucinations in schizophrenia. *J Neurosci*, *34*(24), 8072-8082. https://doi.org/10.1523/JNEUROSCI.0200-14.2014

Huang, A. S., Kang, K., Vandekar, S., Rogers, B. P., Heckers, S., & Woodward, N. D. (2024). Lifespan development of thalamic nuclei and characterizing thalamic nuclei abnormalities in schizophrenia using normative modeling. *Neuropsychopharmacology*. https://doi.org/10.1038/s41386-024-01837-y

Iglesias, J. E., Insausti, R., Lerma-Usabiaga, G., Bocchetta, M., Van Leemput, K., Greve, D. N., van der Kouwe, A., Alzheimer's Disease Neuroimaging, I., Fischl, B., Caballero-Gaudes, C., & Paz-Alonso, P. M. (2018). A probabilistic atlas of the human thalamic nuclei combining ex vivo MRI and histology. *Neuroimage*, *183*, 314-326. https://doi.org/10.1016/j.neuroimage.2018.08.012

Inan, S., Mitchell, T., Song, A., Bizzell, J., & Belger, A. (2004). Hemodynamic correlates of stimulus repetition in the visual and auditory cortices: an fMRI study. *Neuroimage*, *21*(3), 886-893. https://doi.org/10.1016/j.neuroimage.2003.10.029

Ito, T., Bishop, D. C., & Oliver, D. L. (2016). Functional organization of the local circuit in the inferior colliculus. *Anat Sci Int*, *91*(1), 22-34. https://doi.org/10.1007/s12565-015-0308-8

Jacoby, N., Bruneau, E., Koster-Hale, J., & Saxe, R. (2016). Localizing Pain Matrix and Theory of Mind networks with both verbal and non-verbal stimuli. *Neuroimage*, *126*, 39-48. https://doi.org/10.1016/j.neuroimage.2015.11.025

Jiang, F., Stecker, G. C., & Fine, I. (2013). Functional localization of the auditory thalamus in individual human subjects. *Neuroimage*, *78*, 295-304. https://doi.org/10.1016/j.neuroimage.2013.04.035

Johnson, W. E., Li, C., & Rabinovic, A. (2007). Adjusting batch effects in microarray expression data using empirical Bayes methods. *Biostatistics*, *8*(1), 118-127. https://doi.org/10.1093/biostatistics/kxj037

Jones, E. G. (2007). *The thalamus* (2nd ed.). Cambridge University Press.

Kandel, E. R. (2013). *Principles of neural science* (5th ed.). McGraw-Hill.

Karlsgodt, K. H. (2016). Diffusion Imaging of White Matter In Schizophrenia: Progress and Future Directions. *Biol Psychiatry Cogn Neurosci Neuroimaging*, *1*(3), 209-217. https://doi.org/10.1016/j.bpsc.2015.12.001

Kastner, S., O'Connor, D. H., Fukui, M. M., Fehd, H. M., Herwig, U., & Pinsk, M. A. (2004). Functional imaging of the human lateral geniculate nucleus and pulvinar. *J Neurophysiol*, *91*(1), 438-448. https://doi.org/10.1152/jn.00553.2003

Kastner, S., Schneider, K. A., & Wunderlich, K. (2006). Beyond a relay nucleus: neuroimaging views on the human LGN. *Prog Brain Res*, *155*, 125-143. https://doi.org/10.1016/S0079-6123(06)55008-3

Kay, S. R., Fiszbein, A., & Opler, L. A. (1987). The positive and negative syndrome scale (PANSS) for schizophrenia. *Schizophr Bull*, *13*(2), 261-276. http://www.ncbi.nlm.nih.gov/pubmed/3616518

Keil, B., Blau, J. N., Biber, S., Hoecht, P., Tountcheva, V., Setsompop, K., Triantafyllou, C., & Wald, L. L. (2013). A 64-channel 3T array coil for accelerated brain MRI. *Magn Reson Med*, *70*(1), 248-258. https://doi.org/10.1002/mrm.24427

Kelly, S., Jahanshad, N., Zalesky, A., Kochunov, P., Agartz, I., Alloza, C., Andreassen, O. A., Arango, C., Banaj, N., Bouix, S., Bousman, C. A., Brouwer, R. M., Bruggemann, J., Bustillo, J., Cahn, W., Calhoun, V., Cannon, D., Carr, V., Catts, S.,…Donohoe, G. (2018). Widespread white matter microstructural differences in schizophrenia across 4322 individuals: results from the ENIGMA Schizophrenia DTI Working Group. *Mol Psychiatry*, *23*(5), 1261-1269. https://doi.org/10.1038/mp.2017.170

Kendall, M. G. (1990). *Rank Correlation Methods*. E. Arnold; Oxford University Press. https://archive.org/details/rankcorrelationm0000kend

Kim, J. B., Suh, S. I., Seo, W. K., Oh, K., Koh, S. B., & Kim, J. H. (2014). Altered thalamocortical functional connectivity in idiopathic generalized epilepsy. *Epilepsia*, *55*(4), 592-600. https://doi.org/10.1111/epi.12580

Kiwitz, K., Brandstetter, A., Schiffer, C., Bludau, S., Mohlberg, H., Omidyeganeh, M., Massicotte, P., & Amunts, K. (2022). Cytoarchitectonic Maps of the Human Metathalamus in 3D Space. *Front Neuroanat*, *16*, 837485. https://doi.org/10.3389/fnana.2022.837485

Kubota, M., Miyata, J., Sasamoto, A., Sugihara, G., Yoshida, H., Kawada, R., Fujimoto,

S., Tanaka, Y., Sawamoto, N., Fukuyama, H., Takahashi, H., & Murai, T. (2013). Thalamocortical disconnection in the orbitofrontal region associated with cortical thinning in schizophrenia. *JAMA Psychiatry*, *70*(1), 12-21. https://doi.org/10.1001/archgenpsychiatry.2012.1023

Lee, B. B., Martin, P. R., & Grunert, U. (2010). Retinal connectivity and primate vision. *Prog Retin Eye Res*, *29*(6), 622-639. https://doi.org/10.1016/j.preteyeres.2010.08.004

Lee, C. C. (2013). Thalamic and cortical pathways supporting auditory processing. *Brain Lang*, *126*(1), 22-28. https://doi.org/10.1016/j.bandl.2012.05.004

Lee, C. C. (2015). Exploring functions for the non-lemniscal auditory thalamus. *Front Neural Circuits*, *9*, 69. https://doi.org/10.3389/fncir.2015.00069

Lee, C. C., & Winer, J. A. (2008). Connections of cat auditory cortex: II. Commissural system. *J Comp Neurol*, *507*(6), 1901-1919. https://doi.org/10.1002/cne.21614

Li, L., & Ebner, F. F. (2016). Cortex dynamically modulates responses of thalamic relay neurons through prolonged circuit-level disinhibition in rat thalamus in vivo. *J Neurophysiol*, *116*(5), 2368-2382. https://doi.org/10.1152/jn.00424.2016

Mai, J. r. K., & Paxinos, G. (2012). *The human nervous system* (3rd ed.). Elsevier Academic Press.

Maldjian, J. A., Laurienti, P. J., & Burdette, J. H. (2004). Precentral gyrus discrepancy in electronic versions of the Talairach atlas. *Neuroimage*, *21*(1), 450-455. https://doi.org/10.1016/j.neuroimage.2003.09.032

Maldjian, J. A., Laurienti, P. J., Kraft, R. A., & Burdette, J. H. (2003). An automated method for neuroanatomic and cytoarchitectonic atlas-based interrogation of

fMRI data sets. *Neuroimage*, *19*(3), 1233-1239. https://doi.org/10.1016/s1053-8119(03)00169-1

Malmierca, M. S., Anderson, L. A., & Antunes, F. M. (2015). The cortical modulation of stimulus-specific adaptation in the auditory midbrain and thalamus: a potential neuronal correlate for predictive coding. *Front Syst Neurosci*, *9*, 19. https://doi.org/10.3389/fnsys.2015.00019

Marcus, D. S., Harwell, J., Olsen, T., Hodge, M., Glasser, M. F., Prior, F., Jenkinson, M., Laumann, T., Curtiss, S. W., & Van Essen, D. C. (2011). Informatics and data mining tools and strategies for the human connectome project. *Front Neuroinform*, *5*, 4. https://doi.org/10.3389/fninf.2011.00004

Milne, B. J., Caspi, A., Crump, R., Poulton, R., Rutter, M., Sears, M. R., & Moffitt, T. E. (2009). The validity of the family history screen for assessing family history of mental disorders. *Am J Med Genet B Neuropsychiatr Genet*, *150B*(1), 41-49. https://doi.org/10.1002/ajmg.b.30764

Moeller, S., Yacoub, E., Olman, C. A., Auerbach, E., Strupp, J., Harel, N., & Ugurbil, K. (2010). Multiband multislice GE-EPI at 7 tesla, with 16-fold acceleration using partial parallel imaging with application to high spatial and temporal whole-brain fMRI. *Magn Reson Med*, *63*(5), 1144-1153. https://doi.org/10.1002/mrm.22361

Muller-Axt, C., Eichner, C., Rusch, H., Kauffmann, L., Bazin, P. L., Anwander, A., Morawski, M., & von Kriegstein, K. (2021). Mapping the human lateral geniculate nucleus and its cytoarchitectonic subdivisions using quantitative MRI. *Neuroimage*, *244*, 118559. https://doi.org/10.1016/j.neuroimage.2021.118559

Murray, J. D., & Anticevic, A. (2017). Toward understanding thalamocortical dysfunction

in schizophrenia through computational models of neural circuit dynamics. *Schizophr Res*, *180*, 70-77. https://doi.org/10.1016/j.schres.2016.10.021

Oishi, H., Takemura, H., & Amano, K. (2023). Macromolecular tissue volume mapping of lateral geniculate nucleus subdivisions in living human brains. *Neuroimage*, *265*, 119777. https://doi.org/10.1016/j.neuroimage.2022.119777

Oldfield, R. C. (1971). The assessment and analysis of handedness: the Edinburgh inventory. *Neuropsychologia*, *9*(1), 97-113. https://doi.org/10.1016/0028-3932(71)90067-4

Papadopoulou, A., Gaetano, L., Pfister, A., Altermatt, A., Tsagkas, C., Morency, F., Brandt, A. U., Hardmeier, M., Chakravarty, M. M., Descoteaux, M., Kappos, L., Sprenger, T., & Magon, S. (2019). Damage of the lateral geniculate nucleus in MS: Assessing the missing node of the visual pathway. *Neurology*, *92*(19), e2240-e2249. https://doi.org/10.1212/WNL.0000000000007450

Parkes, L. M., Schwarzbach, J. V., Bouts, A. A., Deckers, R. H., Pullens, P., Kerskens, C. M., & Norris, D. G. (2005). Quantifying the spatial resolution of the gradient echo and spin echo BOLD response at 3 Tesla. *Magn Reson Med*, *54*(6), 1465-1472. https://doi.org/10.1002/mrm.20712

Parras, G. G., Nieto-Diego, J., Carbajal, G. V., Valdes-Baizabal, C., Escera, C., & Malmierca, M. S. (2017). Neurons along the auditory pathway exhibit a hierarchical organization of prediction error. *Nat Commun*, *8*(1), 2148. https://doi.org/10.1038/s41467-017-02038-6

Pasternak, O., Kelly, S., Sydnor, V. J., & Shenton, M. E. (2018). Advances in microstructural diffusion neuroimaging for psychiatric disorders. *Neuroimage*.

https://doi.org/10.1016/j.neuroimage.2018.04.051

Peirce, J., Gray, J. R., Simpson, S., MacAskill, M., Hochenberger, R., Sogo, H., Kastman, E., & Lindelov, J. K. (2019). PsychoPy2: Experiments in behavior made easy. *Behav Res Methods*, *51*(1), 195-203. https://doi.org/10.3758/s13428-018-01193-y

Peirce, J. W. (2007). PsychoPy--Psychophysics software in Python. *J Neurosci Methods*, *162*(1-2), 8-13. https://doi.org/10.1016/j.jneumeth.2006.11.017

Peirce, J. W. (2008). Generating Stimuli for Neuroscience Using PsychoPy. *Front Neuroinform*, *2*, 10. https://doi.org/10.3389/neuro.11.010.2008

Peters, S. K., Dunlop, K., & Downar, J. (2016). Cortico-Striatal-Thalamic Loop Circuits of the Salience Network: A Central Pathway in Psychiatric Disease and Treatment. *Front Syst Neurosci*, *10*, 104. https://doi.org/10.3389/fnsys.2016.00104

Pettersson-Yeo, W., Allen, P., Benetti, S., McGuire, P., & Mechelli, A. (2011). Dysconnectivity in schizophrenia: where are we now? *Neurosci Biobehav Rev*, *35*(5), 1110-1124. https://doi.org/10.1016/j.neubiorev.2010.11.004

Power, J. D., Barnes, K. A., Snyder, A. Z., Schlaggar, B. L., & Petersen, S. E. (2012). Spurious but systematic correlations in functional connectivity MRI networks arise from subject motion. *Neuroimage*, *59*(3), 2142-2154. https://doi.org/10.1016/j.neuroimage.2011.10.018

Power, J. D., Mitra, A., Laumann, T. O., Snyder, A. Z., Schlaggar, B. L., & Petersen, S. E. (2014). Methods to detect, characterize, and remove motion artifact in resting state fMRI. *Neuroimage*, *84*, 320-341.

https://doi.org/10.1016/j.neuroimage.2013.08.048

Power, J. D., Schlaggar, B. L., & Petersen, S. E. (2015). Recent progress and outstanding issues in motion correction in resting state fMRI. *Neuroimage*, *105*, 536-551. https://doi.org/10.1016/j.neuroimage.2014.10.044

Rademacher, J., Burgel, U., & Zilles, K. (2002). Stereotaxic localization, intersubject variability, and interhemispheric differences of the human auditory thalamocortical system. *Neuroimage*, *17*(1), 142-160. https://doi.org/10.1006/nimg.2002.1178

Ramachandra, V., Pawlak, V., Wallace, D. J., & Kerr, J. N. D. (2020). Impact of visual callosal pathway is dependent upon ipsilateral thalamus. *Nat Commun*, *11*(1), 1889. https://doi.org/10.1038/s41467-020-15672-4

Robinson, E. C., Garcia, K., Glasser, M. F., Chen, Z., Coalson, T. S., Makropoulos, A., Bozek, J., Wright, R., Schuh, A., Webster, M., Hutter, J., Price, A., Cordero Grande, L., Hughes, E., Tusor, N., Bayly, P. V., Van Essen, D. C., Smith, S. M., Edwards, A. D.,…Rueckert, D. (2018). Multimodal surface matching with higher-order smoothness constraints. *Neuroimage*, *167*, 453-465. https://doi.org/10.1016/j.neuroimage.2017.10.037

Robinson, E. C., Jbabdi, S., Glasser, M. F., Andersson, J., Burgess, G. C., Harms, M. P., Smith, S. M., Van Essen, D. C., & Jenkinson, M. (2014). MSM: a new flexible framework for Multimodal Surface Matching. *Neuroimage*, *100*, 414-426. https://doi.org/10.1016/j.neuroimage.2014.05.069

Rosa, M. J., Kilner, J., Blankenburg, F., Josephs, O., & Penny, W. (2010). Estimating the transfer function from neuronal activity to BOLD using simultaneous EEG-

fMRI. *Neuroimage*, *49*(2), 1496-1509. https://doi.org/10.1016/j.neuroimage.2009.09.011

Saxe, R., Brett, M., & Kanwisher, N. (2006). Divide and conquer: a defense of functional localizers. *Neuroimage*, *30*(4), 1088-1096; discussion 1097-1089. https://doi.org/10.1016/j.neuroimage.2005.12.062

Schmid, M. C., Mrowka, S. W., Turchi, J., Saunders, R. C., Wilke, M., Peters, A. J., Ye, F. Q., & Leopold, D. A. (2010). Blindsight depends on the lateral geniculate nucleus. *Nature*, *466*(7304), 373-377. https://doi.org/10.1038/nature09179

Schmidt, C. F., Zaehle, T., Meyer, M., Geiser, E., Boesiger, P., & Jancke, L. (2008). Silent and continuous fMRI scanning differentially modulate activation in an auditory language comprehension task. *Hum Brain Mapp*, *29*(1), 46-56. https://doi.org/10.1002/hbm.20372

Schneider, K. A., & Kastner, S. (2009). Effects of sustained spatial attention in the human lateral geniculate nucleus and superior colliculus. *J Neurosci*, *29*(6), 1784-1795. https://doi.org/10.1523/JNEUROSCI.4452-08.2009

Serrano-Sosa, M., Van Snellenberg, J. X., Meng, J., Luceno, J. R., Spuhler, K., Weinstein, J. J., Abi-Dargham, A., Slifstein, M., & Huang, C. (2021). Multitask Learning Based Three-Dimensional Striatal Segmentation of MRI: fMRI and PET Objective Assessments. *J Magn Reson Imaging*, *54*(5), 1623-1635. https://doi.org/10.1002/jmri.27682

Sheffield, J. M., Huang, A. S., Rogers, B. P., Giraldo-Chica, M., Landman, B. A., Blackford, J. U., Heckers, S., & Woodward, N. D. (2020). Thalamocortical Anatomical Connectivity in Schizophrenia and Psychotic Bipolar Disorder.

Schizophr Bull, *46*(5), 1062-1071. https://doi.org/10.1093/schbul/sbaa022

Sherman, S. M. (2016). Thalamus plays a central role in ongoing cortical functioning. *Nat Neurosci*, *19*(4), 533-541. https://doi.org/10.1038/nn.4269

Shmuel, A., Yacoub, E., Chaimow, D., Logothetis, N. K., & Ugurbil, K. (2007). Spatio-temporal point-spread function of fMRI signal in human gray matter at 7 Tesla. *Neuroimage*, *35*(2), 539-552. https://doi.org/10.1016/j.neuroimage.2006.12.030

Sitek, K. R., Gulban, O. F., Calabrese, E., Johnson, G. A., Lage-Castellanos, A., Moerel, M., Ghosh, S. S., & De Martino, F. (2019). Mapping the human subcortical auditory system using histology, postmortem MRI and in vivo MRI at 7T. *Elife*, *8*. https://doi.org/10.7554/eLife.48932

Smith, S. M., & Nichols, T. E. (2009). Threshold-free cluster enhancement: addressing problems of smoothing, threshold dependence and localisation in cluster inference. *Neuroimage*, *44*(1), 83-98. https://doi.org/10.1016/j.neuroimage.2008.03.061

Smyser, C. D., Snyder, A. Z., & Neil, J. J. (2011). Functional connectivity MRI in infants: exploration of the functional organization of the developing brain. *Neuroimage*, *56*(3), 1437-1452. https://doi.org/10.1016/j.neuroimage.2011.02.073

Su, J. H., Thomas, F. T., Kasoff, W. S., Tourdias, T., Choi, E. Y., Rutt, B. K., & Saranathan, M. (2019). Thalamus Optimized Multi Atlas Segmentation (THOMAS): fast, fully automated segmentation of thalamic nuclei from structural MRI. *Neuroimage*, *194*, 272-282. https://doi.org/10.1016/j.neuroimage.2019.03.021

Tagliazucchi, E., & Laufs, H. (2014). Decoding wakefulness levels from typical fMRI

resting-state data reveals reliable drifts between wakefulness and sleep. *Neuron*, *82*(3), 695-708. https://doi.org/10.1016/j.neuron.2014.03.020

Tamnes, C. K., & Agartz, I. (2016). White Matter Microstructure in Early-Onset Schizophrenia: A Systematic Review of Diffusion Tensor Imaging Studies. *J Am Acad Child Adolesc Psychiatry*, *55*(4), 269-279. https://doi.org/10.1016/j.jaac.2016.01.004

Tourdias, T., Saranathan, M., Levesque, I. R., Su, J., & Rutt, B. K. (2014). Visualization of intra-thalamic nuclei with optimized white-matter-nulled MPRAGE at 7T. *Neuroimage*, *84*, 534-545. https://doi.org/10.1016/j.neuroimage.2013.08.069

Truong, D. T., Rendall, A. R., Castelluccio, B. C., Eigsti, I. M., & Fitch, R. H. (2015). Auditory processing and morphological anomalies in medial geniculate nucleus of Cntnap2 mutant mice. *Behav Neurosci*, *129*(6), 731-743. https://doi.org/10.1037/bne0000096

Tu, P. C., Bai, Y. M., Li, C. T., Chen, M. H., Lin, W. C., Chang, W. C., & Su, T. P. (2019). Identification of Common Thalamocortical Dysconnectivity in Four Major Psychiatric Disorders. *Schizophr Bull*, *45*(5), 1143-1151. https://doi.org/10.1093/schbul/sby166

Ugurbil, K. (2016). What is feasible with imaging human brain function and connectivity using functional magnetic resonance imaging. *Philos Trans R Soc Lond B Biol Sci*, *371*(1705). https://doi.org/10.1098/rstb.2015.0361

Ugurbil, K., Xu, J., Auerbach, E. J., Moeller, S., Vu, A. T., Duarte-Carvajalino, J. M., Lenglet, C., Wu, X., Schmitter, S., Van de Moortele, P. F., Strupp, J., Sapiro, G., De Martino, F., Wang, D., Harel, N., Garwood, M., Chen, L., Feinberg, D. A.,

Smith, S. M.,…Consortium, W. U.-M. H. (2013). Pushing spatial and temporal resolution for functional and diffusion MRI in the Human Connectome Project. *Neuroimage*, *80*, 80-104. https://doi.org/10.1016/j.neuroimage.2013.05.012

van der Knaap, L. J., & van der Ham, I. J. (2011). How does the corpus callosum mediate interhemispheric transfer? A review. *Behav Brain Res*, *223*(1), 211-221. https://doi.org/10.1016/j.bbr.2011.04.018

van Doorn, J., Westfall, H. A., & Lee, M. D. (2021). Using the Weighted Kendall Distance to Analyze Rank Data in Psychology. *The Quantitative Methods for Psychology*, *17*(2), 154-165. https://doi.org/10.20982/tqmp.17.2.p154

Vu, A. T., Jamison, K., Glasser, M. F., Smith, S. M., Coalson, T., Moeller, S., Auerbach, E. J., Ugurbil, K., & Yacoub, E. (2017). Tradeoffs in pushing the spatial resolution of fMRI for the 7T Human Connectome Project. *Neuroimage*, *154*, 23-32. https://doi.org/10.1016/j.neuroimage.2016.11.049

Ward, L. M. (2013). The thalamus: gateway to the mind. *Wiley Interdiscip Rev Cogn Sci*, *4*(6), 609-622. https://doi.org/10.1002/wcs.1256

Wepsic, J. G. (1966). Multimodal sensory activation of cells in the magnocellular medial geniculate nucleus. *Exp Neurol*, *15*(3), 299-318. https://doi.org/10.1016/0014-4886(66)90053-7

Williams, J. C., Tubiolo, P. N., Luceno, J. R., & Van Snellenberg, J. X. (2022). Advancing motion denoising of multiband resting-state functional connectivity fMRI data. *Neuroimage*, 118907. https://doi.org/10.1016/j.neuroimage.2022.118907

Williams, J. C., Tubiolo, P. N., Nizambad, S., Patel, Y., Zheng, Z. J., Silver-Frankel, E.

B., Pham, D. T., Haubold, N. K., Abeykoon, S. K., Abi-Dargham, A., Horga, G., & Van Snellenberg, J. X. (2024). *Auditory and visual sensory thalamic localizer task* (Version 1.0.0) [Computer software]. Available from https://github.com/CNaP-Lab/Sensory-Thalamic-Localizer and http://www.neurobs.com/ex_files/expt_view?id=302.

Winkler, A. M., Ridgway, G. R., Douaud, G., Nichols, T. E., & Smith, S. M. (2016). Faster permutation inference in brain imaging. *Neuroimage*, *141*, 502-516. https://doi.org/10.1016/j.neuroimage.2016.05.068

Winkler, A. M., Ridgway, G. R., Webster, M. A., Smith, S. M., & Nichols, T. E. (2014). Permutation inference for the general linear model. *Neuroimage*, *92*, 381-397. https://doi.org/10.1016/j.neuroimage.2014.01.060

Winkler, A. M., Webster, M. A., Brooks, J. C., Tracey, I., Smith, S. M., & Nichols, T. E. (2016). Non-parametric combination and related permutation tests for neuroimaging. *Hum Brain Mapp*, *37*(4), 1486-1511. https://doi.org/10.1002/hbm.23115

Winkler, A. M., Webster, M. A., Vidaurre, D., Nichols, T. E., & Smith, S. M. (2015). Multi-level block permutation. *Neuroimage*, *123*, 253-268. https://doi.org/10.1016/j.neuroimage.2015.05.092

Woodward, N. D., & Cascio, C. J. (2015). Resting-State Functional Connectivity in Psychiatric Disorders. *JAMA Psychiatry*, *72*(8), 743-744. https://doi.org/10.1001/jamapsychiatry.2015.0484

Woodward, N. D., Giraldo-Chica, M., Rogers, B., & Cascio, C. J. (2017). Thalamocortical dysconnectivity in autism spectrum disorder: An analysis of the

Autism Brain Imaging Data Exchange. *Biol Psychiatry Cogn Neurosci Neuroimaging*, *2*(1), 76-84. https://doi.org/10.1016/j.bpsc.2016.09.002

Woodward, N. D., & Heckers, S. (2016). Mapping Thalamocortical Functional Connectivity in Chronic and Early Stages of Psychotic Disorders. *Biol Psychiatry*, *79*(12), 1016-1025. https://doi.org/10.1016/j.biopsych.2015.06.026

Woodward, N. D., Karbasforoushan, H., & Heckers, S. (2012). Thalamocortical dysconnectivity in schizophrenia. *Am J Psychiatry*, *169*(10), 1092-1099. https://doi.org/10.1176/appi.ajp.2012.12010056

Yang, Y., Engelien, A., Engelien, W., Xu, S., Stern, E., & Silbersweig, D. A. (2000). A silent event-related functional MRI technique for brain activation studies without interference of scanner acoustic noise. *Magn Reson Med*, *43*(2), 185-190. https://doi.org/10.1002/(sici)1522-2594(200002)43:2<185::aid-mrm4>3.0.co;2-3

Yu, M., Linn, K. A., Cook, P. A., Phillips, M. L., McInnis, M., Fava, M., Trivedi, M. H., Weissman, M. M., Shinohara, R. T., & Sheline, Y. I. (2018). Statistical harmonization corrects site effects in functional connectivity measurements from multi-site fMRI data. *Hum Brain Mapp*, *39*(11), 4213-4227. https://doi.org/10.1002/hbm.24241

Zaehle, T., Schmidt, C. F., Meyer, M., Baumann, S., Baltes, C., Boesiger, P., & Jancke, L. (2007). Comparison of "silent" clustered and sparse temporal fMRI acquisitions in tonal and speech perception tasks. *Neuroimage*, *37*(4), 1195-1204. https://doi.org/10.1016/j.neuroimage.2007.04.073